

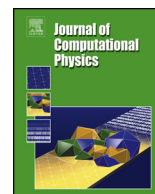


ELSEVIER

Contents lists available at ScienceDirect

Journal of Computational Physics

www.elsevier.com/locate/jcp



High order well-balanced CDG–FE methods for shallow water waves by a Green–Naghdi model

Maojun Li ^{a,b,1}, Philippe Guyenne ^c, Fengyan Li ^d, Liwei Xu ^{a,b,*}^a College of Mathematics and Statistics, Chongqing University, Chongqing, 401331, PR China^b Institute of Scientific and Engineering Computing, Chongqing University, Chongqing, 400044, PR China^c Department of Mathematical Sciences, University of Delaware, Newark, DE 19716-2553, USA^d Department of Mathematical Sciences, Rensselaer Polytechnic Institute, Troy, NY 12180-3590, USA

ARTICLE INFO

Article history:

Received 18 September 2012

Received in revised form 24 July 2013

Accepted 25 September 2013

Available online 2 October 2013

Keywords:

Green–Naghdi equations

Variable bottom topography

Shallow water waves

Central discontinuous Galerkin methods

Well-balanced schemes

Finite element methods

High order methods

ABSTRACT

In this paper, we consider a one-dimensional fully nonlinear weakly dispersive Green–Naghdi model for shallow water waves over variable bottom topographies. Such model describes a large spectrum of shallow water waves, and it is thus of great importance to design accurate and robust numerical methods for solving it. The governing equations contain mixed spatial and temporal derivatives of the unknowns. They also have still-water stationary solutions which should be preserved in stable numerical simulations. In our numerical approach, we first reformulate the Green–Naghdi equations into balance laws coupled with an elliptic equation. We then propose a family of high order numerical methods which discretize the balance laws with well-balanced central discontinuous Galerkin methods and the elliptic part with continuous finite element methods. Linear dispersion analysis for both the (reformulated) Green–Naghdi system and versions of the proposed numerical scheme is performed when the bottom topography is flat. Numerical tests are presented to illustrate the accuracy and stability of the proposed schemes as well as the capability of the Green–Naghdi model to describe a wide range of shallow water wave phenomena.

© 2013 Elsevier Inc. All rights reserved.

1. Introduction

Despite the rapid development in recent years of numerical methods that directly solve the Euler equations for water waves [18–20,44,7], simplified long-wave models of shallow water and Boussinesq type still remain the preferred choice for applications in such areas as coastal and hydraulic engineering. Shallow water (or Saint-Venant) equations can model the propagation of strongly nonlinear waves up to breaking and runup in nearshore zones. However, they fail to properly describe wave propagation in deeper water because they do not incorporate frequency dispersion. Boussinesq systems carry weak frequency dispersion but are typically restricted to small-amplitude waves. In the past few decades, much effort has been devoted to improve their dispersive and nonlinear properties and, as a result, the current generation of Boussinesq models has reached a high degree of sophistication, being applicable to highly nonlinear waves, shorter wavelengths and deeper water [1,15,13,34].

Extensions of the shallow water equations that incorporate frequency dispersion can be traced back to Serre [33] who derived a one-dimensional system of equations for fully nonlinear weakly dispersive waves over flat bottom (see also [35]).

* Corresponding author at: College of Mathematics and Statistics, Chongqing University, Chongqing, 401331, PR China.

E-mail addresses: limaojun216@gmail.com (M. Li), guyenne@math.udel.edu (P. Guyenne), lif@rpi.edu (F. Li), xul@cqu.edu.cn (L. Xu).

¹ Maojun Li is currently at Beijing Computational Science Research Center, Beijing 100084, PR China.

Green and Naghdi [17] presented the two-dimensional counterpart of these equations for wave propagation over variable bottom topography. Israwi [21] derived and analyzed a new two-dimensional Green–Naghdi system which allows control of the rotational part of the horizontal velocity. Because so-called Green–Naghdi equations combine both full nonlinearity (i.e. no assumption is made on the wave amplitude) and weak dispersion, they are applicable to a wide range of problems involving small- to large-amplitude waves on both shallow and relatively deep water. For these reasons, there has been increasing interest in the development and simulation of Green–Naghdi models in recent years [8,9,23,31,3,4,6], and this is also the motivation of the present work.

One challenge in developing numerical methods for the Green–Naghdi model is related to the newly added spatial and temporal mixed derivative terms resulting from the inclusion of dispersive effects. To treat such terms, the original Green–Naghdi model is usually reformulated and discretized by hybrid schemes [8,23,3]. This framework is followed in the present work. More specifically, we reformulate the Green–Naghdi equations into balance laws coupled with an elliptic equation by introducing a new unknown instead of working with the traditional one, hu , where h is the total water depth and u is the vertically averaged horizontal velocity. The resulting system is then discretized by a hybrid method combining central discontinuous Galerkin (CDG) methods [27] and continuous finite element (FE) methods. The technique we adopt to reformulate the equations by introducing a new unknown was used in [23] for flat bottom. We here extend it to variable bottom topography. Our reformulation is also close to that in [8] where the original Green–Naghdi model with a dispersion correction term is reformulated into a quasi-conservative system coupled with an elliptic equation using an auxiliary unknown similar to ours. The balance law in the present work has a nontrivial source term which needs special treatment in order to achieve a well-balanced scheme.

In this regard, another issue in simulating Green–Naghdi equations over variable bottom topography is to exactly preserve their still-water stationary wave solution [2]

$$u = 0, \quad h + b = \text{constant}, \quad (1)$$

where b represents the bottom topography and $h + b$ is called the water surface. Numerical schemes exactly preserving the still-water stationary solution are called well-balanced methods. Absence of the well-balanced treatment may introduce oscillations into the approximate solution when it is in or close to a stationary state. For hyperbolic shallow water equations, many high order well-balanced methods have been developed [37–42,30]. In this paper, we propose high order well-balanced methods for a Green–Naghdi model based on the coupled CDG–FE schemes mentioned above. The main ingredient to achieve the well-balanced property is to modify the source term through a special decomposition similar to that proposed in [42]. The resulting spatial discretization has the features of being both high order accurate for general solutions and exactly preserving the still-water stationary solution. In physically relevant numerical simulations, it is also important to preserve the positivity of the water height at all times. A positivity-preserving well-balanced DG scheme solving the classical shallow water equations was recently reported in [43]. Motivated by this work, the development of a positivity-preserving well-balanced CDG scheme for the Green–Naghdi model is currently under way.

The underlying CDG methods are a family of high order numerical methods defined on overlapping meshes, which were originally introduced for hyperbolic conservation laws [27] and then for diffusion equations [28]. These methods can be systematically formulated with any order of (formal) accuracy. By evolving two sets of numerical solutions without using any numerical flux at element interfaces as in Godunov schemes, CDG methods provide new opportunities to designing accurate and stable schemes such as for Hamilton–Jacobi equations [24] and for ideal MHD equations [25,26]. These methods prove again in the present work that they are a good candidate to solve the balance laws resulting from the reformulation of the Green–Naghdi model (see Section 3.1) without explicitly “knowing” a lot about the equations, and to achieve the well-balanced property of the overall scheme.

After the proposed well-balanced CDG–FE schemes are formulated, their performance and reliability will be demonstrated through a sequence of numerical tests. Moreover, we will validate the Green–Naghdi model by comparing with real data from laboratory experiments in coastal engineering. The remainder of the paper is organized as follows. In Section 2, we present the mathematical formulation of the governing equations. Section 3 is devoted to the numerical methods. We first reformulate the equations, and then propose a family of high order schemes which couple well-balanced CDG methods and continuous finite element methods. In Section 4, we analyze the linear dispersion relation for the (reformulated) Green–Naghdi model, together with that for the linearized numerical scheme in its semi-discrete form when the bottom topography is flat. Then, a set of numerical experiments are presented to illustrate the accuracy and well-balanced property of the methods in Section 5. Finally, concluding remarks are given in Section 6.

2. Mathematical formulation: the Green–Naghdi model

We consider the one-dimensional system for fully nonlinear weakly dispersive waves [17,32],

$$\begin{cases} h_t + (hu)_x = 0, \\ (hu)_t + \left(hu^2 + \frac{1}{2}gh^2 + \frac{1}{3}h^3\Phi + \frac{1}{2}h^2\Psi \right)_x = - \left(gh + \frac{1}{2}h^2\Phi + h\Psi \right) b_x, \end{cases} \quad (2)$$

on the domain $\Omega = (x_{\min}, x_{\max})$, with

$$\Phi = -u_{xt} - uu_{xx} + u_x^2, \quad \Psi = b_x u_t + b_x u u_x + b_{xx} u^2, \tag{3}$$

where h is the total water depth, u is the vertically averaged horizontal velocity, g is the gravitational constant, and b is the bottom topography. The subscripts t and x denote the partial derivatives with respect to the time variable t and the spatial variable x , respectively. For flat bottom, meaning $b(x)$ is constant, system (2) becomes

$$\begin{cases} h_t + (hu)_x = 0, \\ (hu)_t + \left(hu^2 + \frac{1}{2}gh^2 + \frac{1}{3}h^3\Phi \right)_x = 0, \end{cases} \tag{4}$$

which was first derived by Serre [33] and then rederived by Su and Gardner [35]. We refer to system (2) (resp. (4)) as Green–Naghdi equations for a non-flat (resp. flat) bottom. If $\Phi = \Psi = 0$, then (2) and (4) coincide with the classical shallow water equations for non-flat and flat bottom topography, respectively.

One difficulty in designing numerical schemes for the Green–Naghdi model comes from the mixed spatial and temporal derivatives in the equations. To tackle this, we first reformulate the original equations, as described in Section 3.1. Moreover, in the case of variable bottom, system (2) has a still-water stationary solution (1) for which the flux term is nonzero yet it is exactly balanced by the source term. This balance law however is often violated in standard numerical methods, which may lead to oscillations when the solution is in or close to a stationary state. In the present work, a new well-balanced scheme based on CDG methods is proposed in Section 3.2.2 which exactly preserves the still-water stationary solution (1).

3. Numerical schemes

3.1. Reformulation of the Green–Naghdi model

In order to treat the mixed spatial and temporal derivatives in (2), we first introduce a new unknown

$$hK = -\frac{1}{3}(h^3 u_x)_x + h \left(1 + h_x b_x + \frac{1}{2} h b_{xx} + b_x^2 \right) u. \tag{5}$$

Note that the terms containing Φ and Ψ in (2) can be rewritten as

$$\begin{cases} \frac{1}{3}h^3\Phi = -\left(\frac{1}{3}h^3u_x\right)_t - \left(\frac{1}{3}h^3u_x\right)_x u - \frac{2}{3}h^3u_x^2, \\ \frac{1}{2}h^2b_x\Phi = -\left(\frac{1}{2}h^2b_xu_x\right)_t - hh_xb_xuu_x - \frac{1}{2}h^2b_xuu_{xx} - \frac{1}{2}h^2b_xu_x^2, \\ \frac{1}{2}h^2\Psi = \left(\frac{1}{2}h^2b_xu\right)_t + \frac{1}{2}h^2u^2b_{xx} + hh_xu^2b_x + \frac{3}{2}h^2uu_xb_x, \\ hb_x\Psi = (hb_x^2u)_t + (hu^2b_x^2)_x - hu^2b_xb_{xx}. \end{cases} \tag{6}$$

By applying the identities in (6) and using K , system (2) can be reformulated into a balance law

$$\begin{cases} h_t + (hu)_x = 0, \\ (hK)_t + \left(hKu + \frac{1}{2}gh^2 - \frac{2}{3}h^3u_x^2 + h^2uu_xb_x \right)_x = -ghb_x - \frac{1}{2}h^2uu_xb_{xx} + hu^2b_xb_{xx}, \end{cases} \tag{7}$$

where the conventional unknowns $(h, hu)^T$ are replaced by the new unknowns $(h, hK)^T$. With this new formulation, the solution of the original Green–Naghdi model (2) amounts to finding the unknowns $(h, hK)^T$ based on (7) and the unknown u from (5). Note that Eq. (5) is of elliptic type as long as $h > 0$. In the region where $h = 0$, we impose the solution u to be zero.

For flat bottom, Eqs. (5) and (7) become a coupled system of an elliptic equation

$$hK = -\frac{1}{3}(h^3 u_x)_x + hu, \tag{8}$$

and conservation laws

$$\begin{cases} h_t + (hu)_x = 0, \\ (hK)_t + \left(hKu + \frac{1}{2}gh^2 - \frac{2}{3}h^3u_x^2 \right)_x = 0. \end{cases} \tag{9}$$

From now on, we refer to Eqs. (7) and (5) as the non-flat bottom Green–Naghdi (GN-NFB) model, and to Eqs. (9) and (8) as the flat bottom Green–Naghdi (GN-FB) model. The technique to replace hu by hK was first used in [5] for the Hamiltonian formulation of the Green–Naghdi model, and later in [23] for the Green–Naghdi model with flat bottom.

The unknown K in (8) is an alternative definition for the potential flow of the Green–Naghdi model with flat bottom, and its definition is not unique [23]. In the present paper, the unknown K given in (5) plays a similar role for variable bottom and its definition is not unique either [29]. This auxiliary variable is used for numerical purposes, as in [8] where a fourth-order finite volume method was developed to solve the reformulated Serre equations.

For ease of presentation, we rewrite (7) as

$$\mathbf{U}_t + \mathbf{G}(\mathbf{U}, u; b)_x = \mathbf{S}(\mathbf{U}, u; b), \tag{10}$$

where $\mathbf{U} = (h, hK)^\top$,

$$\mathbf{G}(\mathbf{U}, u; b) = \left(hu, hKu + \frac{1}{2}gh^2 - \frac{2}{3}h^3u_x^2 + h^2uu_xb_x \right)^\top$$

is the flux, and

$$\mathbf{S}(\mathbf{U}, u; b) = \left(0, -ghb_x - \frac{1}{2}h^2uu_xb_{xx} + hu^2b_xb_{xx} \right)^\top$$

is the source term. Note that if we instead replace h_t , the first component of \mathbf{U}_t , by $(h + b)_t$, then Eq. (10) still holds with the same $\mathbf{G}(\mathbf{U}, u; b)$ and $\mathbf{S}(\mathbf{U}, u; b)$ due to the fact that $(h + b)_t = h_t + b_t = h_t$. This observation will be used in formulating the well-balanced schemes in Section 3.2.2. Similarly, Eq. (9) can be rewritten as

$$\mathbf{U}_t + \mathbf{F}(\mathbf{U}, u)_x = 0, \tag{11}$$

with

$$\mathbf{F}(\mathbf{U}, u) = \left(hu, hKu + \frac{1}{2}gh^2 - \frac{2}{3}h^3u_x^2 \right)^\top$$

being the flux.

3.2. Numerical schemes for GN-FB and GN-NFB models

In this section, we develop numerical schemes for the GN-FB and GN-NFB models. Since extra consideration on the balance of the flux and source terms is required for the GN-NFB model, we present numerical schemes for these two models separately. Let $\{x_j\}_j$ be a partition of the computational domain Ω . With $x_{j+\frac{1}{2}} = \frac{1}{2}(x_j + x_{j+1})$, $I_j = (x_{j-\frac{1}{2}}, x_{j+\frac{1}{2}})$ and $I_{j+\frac{1}{2}} = (x_j, x_{j+1})$, we define two discrete function spaces, associated with overlapping meshes $\{I_j\}_j$ and $\{I_{j+\frac{1}{2}}\}_j$, to approximate \mathbf{U} ,

$$\begin{aligned} \mathcal{V}_h^C &= \mathcal{V}_h^{C,k} = \{ \mathbf{v}: \mathbf{v}|_{I_j} \in [P^k(I_j)]^2, \forall j \}, \\ \mathcal{V}_h^D &= \mathcal{V}_h^{D,k} = \{ \mathbf{v}: \mathbf{v}|_{I_{j+\frac{1}{2}}} \in [P^k(I_{j+\frac{1}{2}})]^2, \forall j \}, \end{aligned}$$

where $P^k(I)$ denotes the space of polynomials in I with degree at most k , and $[P^k(I)]^2 = \{ \mathbf{v} = (v_1, v_2)^\top : v_i \in P^k(I), i = 1, 2 \}$ is its vector version. To approximate u , we define two continuous finite element spaces

$$\begin{aligned} \mathcal{W}_h^C &= \mathcal{W}_h^{C,k} = \{ w: w|_{I_j} \in P^k(I_j), \forall j \text{ and } w \text{ is continuous} \}, \\ \mathcal{W}_h^D &= \mathcal{W}_h^{D,k} = \{ w: w|_{I_{j+\frac{1}{2}}} \in P^k(I_{j+\frac{1}{2}}), \forall j \text{ and } w \text{ is continuous} \}. \end{aligned}$$

For simplicity, we present the schemes in the case of the forward Euler method for time discretization. High order time discretizations will be discussed afterward. The proposed methods evolve two copies of numerical solutions, which are assumed to be available at $t = t_n$, denoted by $\mathbf{U}_h^{n,*} = (h_h^{n,*}, (hK)_h^{n,*})^\top \in \mathcal{V}_h^*$ and $u_h^{n,*} \in \mathcal{W}_h^*$, and we want to find the solutions at $t = t_{n+1} = t_n + \Delta t_n$. Hereinafter, the symbol \star denotes C or D . For convenience, we only present the procedure to update $\mathbf{U}_h^{n+1,C}$ and $u_h^{n+1,C}$ as the one for $\mathbf{U}_h^{n+1,D}$ and $u_h^{n+1,D}$ is similar. For the bottom topography function b , we project it onto $P^k(I_j)$ on I_j (resp. into $P^k(I_{j+\frac{1}{2}})$ on $I_{j+\frac{1}{2}}$) in the L^2 sense, and obtain an approximation b_h^C (resp. b_h^D) throughout the domain Ω .

3.2.1. Schemes for GN-FB

To get $\mathbf{U}_h^{n+1,C} = (h_h^{n+1,C}, (hK)_h^{n+1,C})^\top$, we apply to (11) the CDG methods of [27] for space discretization and the forward Euler method for time discretization. That is, to look for $\mathbf{U}_h^{n+1,C} \in \mathcal{V}_h^{C,k}$ such that for any $\mathbf{V} \in \mathcal{V}_h^{C,k}|_{I_j}$ with any j ,

$$\int_{I_j} \mathbf{U}_h^{n+1,C} \cdot \mathbf{V} dx = \int_{I_j} (\theta_n \mathbf{U}_h^{n,D} + (1 - \theta_n) \mathbf{U}_h^{n,C}) \cdot \mathbf{V} dx + \Delta t_n \int_{I_j} \mathbf{F}(\mathbf{U}_h^{n,D}, u_h^{n,D}) \cdot \mathbf{V}_x dx - \Delta t_n [\mathbf{F}(\mathbf{U}_h^{n,D}(x_{j+\frac{1}{2}}), u_h^{n,D}(x_{j+\frac{1}{2}})) \cdot \mathbf{V}(x_{j+\frac{1}{2}}) - \mathbf{F}(\mathbf{U}_h^{n,D}(x_{j-\frac{1}{2}}), u_h^{n,D}(x_{j-\frac{1}{2}})) \cdot \mathbf{V}(x_{j-\frac{1}{2}})]. \quad (12)$$

Here $\theta_n = \Delta t_n / \tau_n \in [0, 1]$ with τ_n being the maximal time step allowed by the CFL restriction at t_n (see [27] and also Section 4) and $\Delta t_n = t_{n+1} - t_n$ being the actual time step in the simulation.

Once $\mathbf{U}_h^{n+1,C}$ is available, we can obtain $u_h^{n+1,C}$ by a continuous finite element method: look for $u_h^{n+1,C} \in \widetilde{\mathcal{W}}_h^{C,k}$ such that for any $v \in \widetilde{\mathcal{W}}_h^{C,k}$,

$$\frac{1}{3} \int_{\Omega} (h_h^{n+1,C})^3 (u_h^{n+1,C})_x v_x dx + \int_{\Omega} h_h^{n+1,C} u_h^{n+1,C} v dx = \int_{\Omega} h_h^{n+1,C} K_h^{n+1,C} v dx. \quad (13)$$

Here $\widetilde{\mathcal{W}}_h^{C,k}$ and $\widehat{\mathcal{W}}_h^{C,k}$ are variants of $\mathcal{W}_h^{C,k}$ with consideration of the boundary conditions. For instance, when the boundary condition for u is of Dirichlet type, we use

$$\begin{aligned} \widetilde{\mathcal{W}}_h^{C,k} &= \{w \in \mathcal{W}_h^{C,k}: w \text{ has the same boundary condition as } u\}, \\ \widehat{\mathcal{W}}_h^{C,k} &= \{w \in \mathcal{W}_h^{C,k}: w \text{ has zero boundary condition}\}. \end{aligned}$$

When the boundary condition is periodic, then

$$\widetilde{\mathcal{W}}_h^{C,k} = \widehat{\mathcal{W}}_h^{C,k} = \{w \in \mathcal{W}_h^{C,k}: w(x_{\min}) = w(x_{\max})\}.$$

When the boundary condition is of Neumann type, $\widetilde{\mathcal{W}}_h^{C,k} = \widehat{\mathcal{W}}_h^{C,k} = \mathcal{W}_h^{C,k}$ is taken. The unique solvability of this finite element method can be obtained in a straightforward manner if $h_h^{n+1,C} \geq h_0 > 0$. Though the positivity of $h_h^{n+1,C}$ (and $h_h^{n+1,D}$) is not established for our scheme, all systems resulting from the finite element discretizations reported in Section 5.1 are uniquely solvable. We refer to (12) and (13) as the CDG–FE method.

3.2.2. Well-balanced schemes for GN-NFB

In this subsection, we propose a family of high order well-balanced CDG–FE schemes for the GN-NFB model in (5) and (10), which exactly preserve the still-water steady state solution (1). These schemes involve

- (a) Using $(\eta = h + b, hK)^\top$ as the unknowns in (10) instead of (h, hK) (see also Section 3.1). We denote $(\eta, hK)^\top$ by $\widehat{\mathbf{U}}$. This is not essential, yet when the nonlinear limiter is applied to unknowns $\widehat{\mathbf{U}}$ to ensure numerical stability in Section 3.2.3, the well-balanced property of the overall scheme will not be affected.
- (b) Adding a term to the discretized source term. This guarantees the balance between the flux and source terms in the numerical scheme when solving for the steady state solution (1). This added term is a high order correction when the bottom topography is smooth, hence it will not affect the formal high order accuracy of the scheme.

To get $\widehat{\mathbf{U}}_h^{n+1,C} = (\eta_h^{n+1,C}, (hK)_h^{n+1,C})^\top$, we again first apply to (10) the CDG methods of [27] for space discretization and the forward Euler method for time discretization. That is, to look for $\widehat{\mathbf{U}}_h^{n+1,C} \in \mathcal{V}_h^{C,k}$ such that for any $\mathbf{V} \in \mathcal{V}_h^{C,k}|_{I_j}$ with any j ,

$$\begin{aligned} \int_{I_j} \widehat{\mathbf{U}}_h^{n+1,C} \cdot \mathbf{V} dx &= \int_{I_j} (\theta_n \widehat{\mathbf{U}}_h^{n,D} + (1 - \theta_n) \widehat{\mathbf{U}}_h^{n,C}) \cdot \mathbf{V} dx + \Delta t_n \int_{I_j} \mathbf{G}(\mathbf{U}_h^{n,D}, u_h^{n,D}; b_h^D) \cdot \mathbf{V}_x dx \\ &\quad - \Delta t_n [\mathbf{G}(\mathbf{U}_h^{n,D}(x_{j+\frac{1}{2}}), u_h^{n,D}(x_{j+\frac{1}{2}}); b_h^D(x_{j+\frac{1}{2}})) \cdot \mathbf{V}(x_{j+\frac{1}{2}}) \\ &\quad - \mathbf{G}(\mathbf{U}_h^{n,D}(x_{j-\frac{1}{2}}), u_h^{n,D}(x_{j-\frac{1}{2}}); b_h^D(x_{j-\frac{1}{2}})) \cdot \mathbf{V}(x_{j-\frac{1}{2}})] \\ &\quad + \Delta t_n \int_{I_j} \mathbf{S}(\mathbf{U}_h^{n,D}, u_h^{n,D}; b_h^D) \cdot \mathbf{V} dx, \end{aligned} \quad (14)$$

where θ_n is defined as in Section 3.2.1.

In general, the numerical scheme (14) does not maintain the still-water stationary solution and may produce numerical solutions with spurious oscillations when they are in or close to a stationary state. To achieve the well-balanced property, instead of working with (14), we modify it into the following

$$\begin{aligned} \int_{I_j} \widehat{\mathbf{U}}_h^{n+1,C} \cdot \mathbf{V} dx &= \int_{I_j} (\theta_n \widehat{\mathbf{U}}_h^{n,D} + (1 - \theta_n) \widehat{\mathbf{U}}_h^{n,C}) \cdot \mathbf{V} dx + \Delta t_n \int_{I_j} \mathbf{G}(\mathbf{U}_h^{n,D}, u_h^{n,D}; b_h^D) \cdot \mathbf{V}_x dx \\ &\quad - \Delta t_n [\mathbf{G}(\mathbf{U}_h^{n,D}(x_{j+\frac{1}{2}}), u_h^{n,D}(x_{j+\frac{1}{2}}); b_h^D(x_{j+\frac{1}{2}})) \cdot \mathbf{V}(x_{j+\frac{1}{2}}) \\ &\quad - \mathbf{G}(\mathbf{U}_h^{n,D}(x_{j-\frac{1}{2}}, t), u_h^{n,D}(x_{j-\frac{1}{2}}); b_h^D(x_{j-\frac{1}{2}})) \cdot \mathbf{V}(x_{j-\frac{1}{2}})] \\ &\quad + \Delta t_n \int_{I_j} \mathbf{S}(\mathbf{U}_h^{n,D}, u_h^{n,D}; b_h^D) \cdot \mathbf{V} dx + \Delta t_n \widetilde{\mathbf{S}}(\eta_h^{n,D}; b_h^D) \cdot \mathbf{V}(x_j), \end{aligned} \tag{15}$$

where a new term $\widetilde{\mathbf{S}}(\eta_h^{n,D}; b_h^D)$ is added, which is given by

$$\widetilde{\mathbf{S}}(\eta_h^{n,D}; b_h^D) = \left(0, \frac{g}{2} ((b_h^D(x_j^+))^2 - (b_h^D(x_j^-))^2) - \gamma_j^{n,D} g (b_h^D(x_j^+) - b_h^D(x_j^-)) \right)^\top. \tag{16}$$

Here

$$\gamma_j^{n,D} = \frac{1}{2} (\eta_h^{n,D}(x_{j+\frac{1}{2}}) + \eta_h^{n,D}(x_{j-\frac{1}{2}})),$$

and

$$b_h(x^\pm) = \lim_{\Delta x \rightarrow 0^+} b_h(x \pm \Delta x).$$

To construct a well-balanced scheme, the crucial property of $\gamma_j^{n,D}$ is that in the case of the still-water stationary solution, $\gamma_j^{n,D}$ should be a constant with respect to both j and n . In particular, it should be equal to the constant water surface in (1). Alternatively, we can take

$$\gamma_j^{n,D} = \frac{1}{|I_j|} \int_{I_j} \eta_h^{n,D} dx.$$

Note that the modification by adding the term $\widetilde{\mathbf{S}}$ is of $O(\Delta x^{k+1})$ when the bottom topography function b is sufficiently smooth, and hence it will not affect the (formal) spatial accuracy of standard CDG schemes in (14).

The inclusion of the term $\widetilde{\mathbf{S}}$ is motivated by the following decomposition

$$\begin{aligned} \mathbf{S}(\mathbf{U}_h^{n,D}, u_h^{n,D}; b_h^D) &= \left(0, \frac{g}{2} (b_h^D)^2 - \gamma_j^{n,D} g b_h^D \right)_x^\top - \left(0, g(\eta_h^{n,D} - \gamma_j^{n,D})(b_h^D)_x \right)^\top \\ &\quad + \left(0, h_h^{n,D} (u_h^{n,D})^2 (b_h^D)_x (b_h^D)_{xx} - \frac{1}{2} (h_h^{n,D})^2 u_h^{n,D} (u_h^{n,D})_x (b_h^D)_{xx} \right)^\top, \end{aligned} \tag{17}$$

where $h_h^{n,D}$ is computed from $h_h^{n,D} = \eta_h^{n,D} - b_h^D$. With this, the last two terms in (15) become

$$\begin{aligned} &\Delta t_n \int_{I_j} \mathbf{S}(\mathbf{U}_h^{n,D}, u_h^{n,D}; b_h^D) \cdot \mathbf{V} dx + \Delta t_n \widetilde{\mathbf{S}}(\eta_h^{n,D}; b_h^D) \cdot \mathbf{V}(x_j) \\ &= \Delta t_n \left(0, \frac{g}{2} (b_h^D(x_{j+\frac{1}{2}}))^2 - \gamma_j^{n,D} g b_h^D(x_{j+\frac{1}{2}}) \right)^\top \cdot \mathbf{V}(x_{j+\frac{1}{2}}^-) \\ &\quad - \Delta t_n \left(0, \frac{g}{2} (b_h^D(x_{j-\frac{1}{2}}))^2 - \gamma_j^{n,D} g b_h^D(x_{j-\frac{1}{2}}) \right)^\top \cdot \mathbf{V}(x_{j-\frac{1}{2}}^+) \\ &\quad - \Delta t_n \int_{I_j} \left(0, \frac{g}{2} (b_h^D)^2 - \gamma_j^{n,D} g b_h^D \right)^\top \cdot \mathbf{V}_x dx - \Delta t_n \int_{I_j} \left(0, g(\eta_h^{n,D} - \gamma_j^{n,D})(b_h^D)_x \right)^\top \cdot \mathbf{V} dx \\ &\quad + \Delta t_n \int_{I_j} \left(0, h_h^{n,D} (u_h^{n,D})^2 (b_h^D)_x (b_h^D)_{xx} - \frac{1}{2} (h_h^{n,D})^2 u_h^{n,D} (u_h^{n,D})_x (b_h^D)_{xx} \right)^\top \cdot \mathbf{V} dx, \end{aligned} \tag{18}$$

which is obtained by integrating the first term of (17) by parts, given that b_h^D is discontinuous at x_j . The newly added $\widetilde{\mathbf{S}}$ contributes to canceling terms in this integration by parts. Eq. (18) is used to update $\widehat{\mathbf{U}}_h^{n+1,C}$ in (15).

Once $\widehat{\mathbf{U}}_h^{n+1,C}$ is available, we can obtain $u_h^{n+1,C}$ by again applying a continuous finite element method to (5): look for $u_h^{n+1,C} \in \widehat{\mathcal{W}}_h^{C,k}$ such that for any $v \in \widehat{\mathcal{W}}_h^{C,k}$,

$$\frac{1}{3} \int_{\Omega} (h_h^{n+1,C})^3 (u_h^{n+1,C})_x v_x dx + \int_{\Omega} f(h_h^{n+1,C}; b_h^C) u_h^{n+1,C} v dx = \int_{\Omega} h_h^{n+1,C} K_h^{n+1,C} v dx, \tag{19}$$

where $h_h^{n+1,C} = \eta_h^{n+1,C} - b_h^C$ and

$$f(h_h^{n+1,C}; b_h^C) = h_h^{n+1,C} \left(1 + (h_h^{n+1,C})_x (b_h^C)_x + \frac{1}{2} h_h^{n+1,C} (b_h^C)_{xx} + ((b_h^C)_x)^2 \right). \tag{20}$$

As in Section 3.2.1, $\widehat{\mathcal{W}}_h^{C,k}$ and $\widehat{\mathcal{W}}_h^{D,k}$ are variants of $\mathcal{W}_h^{C,k}$ that take the boundary conditions into account.

In general, the unique solvability of this finite element scheme is more difficult to determine than that of (13) for flat bottom. In all the numerical applications in Section 5.2 we considered, the system for $u_h^{n+1,C}$ (and $u_h^{n+1,D}$) was found to be always uniquely solvable.

Next we turn to the well-balanced property of the proposed scheme. To establish this property, assumptions are made to ensure the unique solvability of the finite element discretization in (19) when the overall scheme is applied to simulating the still-water stationary solution: $h + b = C_0$ and $u = 0$. One set of such assumptions is given below.

(A1) The water height h in the still-water stationary solution considered here has a strictly positive lower bound. That is, there exists a positive constant h_0 such that $h \geq h_0 > 0$.

(A2) With $\star = C$ or D ,

$$1 + \frac{1}{2} h_h^\star (b_h^\star)_{xx} = 1 + \frac{1}{2} (C_0 - b_h^\star) (b_h^\star)_{xx} > 0. \tag{21}$$

Proposition. *The numerical scheme defined in (15) and (19) for the GN-NFB equations (10) and (5) is well-balanced, in the sense that it preserves the still-water stationary solution (1), provided assumptions (A1) and (A2) hold.*

Proof. We start with the still-water solution at $t = 0$, such that the still-water surface $h + b = C_0$, $u = 0$, and the water height h and the bottom topography b satisfy (A1) and (A2). In the initialization step, it is easy to ensure $\widehat{\mathbf{U}}_h^{n,C} = \widehat{\mathbf{U}}_h^{n,D} = (C_0, 0)^\top$ and $u_h^{n,C} = u_h^{n,D} = 0$ for $n = 0$. Suppose $\widehat{\mathbf{U}}_h^{n,C} = \widehat{\mathbf{U}}_h^{n,D} = (C_0, 0)^\top$ and $u_h^{n,C} = u_h^{n,D} = 0$ for $n \geq 0$, we want to establish that the numerical solution computed from (15) and (19) satisfies $\widehat{\mathbf{U}}_h^{n+1,C} = (C_0, 0)^\top$ and $u_h^{n+1,C} = 0$.

Since $\widehat{\mathbf{U}}_h^{n,C} = \widehat{\mathbf{U}}_h^{n,D} = (C_0, 0)^\top$ and $u_h^{n,D} = 0$, the first term on the right-hand side of (15) becomes

$$\int_{I_j} (\theta_n \widehat{\mathbf{U}}_h^{n,D} + (1 - \theta_n) \widehat{\mathbf{U}}_h^{n,C}) \cdot \mathbf{V} dx = \int_{I_j} (C_0, 0)^\top \cdot \mathbf{V} dx, \tag{22}$$

and the flux term is

$$\mathbf{G}(\mathbf{U}_h^{n,D}, u_h^{n,D}; b_h^D) = \left(0, \frac{g}{2} (C_0 - b_h^D)^2 \right)^\top = \left(0, \frac{g}{2} C_0^2 + \frac{g}{2} (b_h^D)^2 - g C_0 b_h^D \right)^\top. \tag{23}$$

With this, the three terms in (15) related to the flux become

$$\begin{aligned} & \Delta t_n \int_{I_j} \mathbf{G}(\mathbf{U}_h^{n,D}, u_h^{n,D}; b_h^D) \cdot \mathbf{V}_x dx - \Delta t_n [\mathbf{G}(\mathbf{U}_h^{n,D}(x_{j+\frac{1}{2}}), u_h^{n,D}(x_{j+\frac{1}{2}}); b_h^D(x_{j+\frac{1}{2}})) \cdot \mathbf{V}(x_{j+\frac{1}{2}}^-) \\ & \quad - \mathbf{G}(\mathbf{U}_h^{n,D}(x_{j-\frac{1}{2}}, t), u_h^{n,D}(x_{j-\frac{1}{2}}); b_h^D(x_{j-\frac{1}{2}})) \cdot \mathbf{V}(x_{j-\frac{1}{2}}^+)] \\ & = \Delta t_n \int_{I_j} \left(0, \frac{g}{2} (b_h^D)^2 - g C_0 b_h^D \right)^\top \cdot \mathbf{V}_x dx - \Delta t_n \left(0, \frac{g}{2} (b_h^D(x_{j+\frac{1}{2}}))^2 - g C_0 b_h^D(x_{j+\frac{1}{2}}) \right)^\top \cdot \mathbf{V}(x_{j+\frac{1}{2}}^-) \\ & \quad + \Delta t_n \left(0, \frac{g}{2} (b_h^D(x_{j-\frac{1}{2}}))^2 - g C_0 b_h^D(x_{j-\frac{1}{2}}) \right)^\top \cdot \mathbf{V}(x_{j-\frac{1}{2}}^+). \end{aligned} \tag{24}$$

In addition, from (18) and the fact that $\gamma_j^{n,D} = C_0$ ($\forall j, n$), the last two terms in (15) are simply

$$\begin{aligned}
 & \Delta t_n \int_{I_j} \mathbf{S}(\mathbf{U}_h^{n,D}, u_h^{n,D}; b_h^D) \cdot \mathbf{V} dx + \Delta t_n \tilde{\mathbf{S}}(\eta_h^{n,D}; b_h^D) \cdot \mathbf{V}(x_j) \\
 &= \Delta t_n \left(0, \frac{g}{2} (b_h^D(x_{j+\frac{1}{2}}))^2 - gC_0 b_h^D(x_{j+\frac{1}{2}}) \right)^\top \cdot \mathbf{V}(x_{j+\frac{1}{2}}) - \Delta t_n \left(0, \frac{g}{2} (b_h^D(x_{j-\frac{1}{2}}))^2 - gC_0 b_h^D(x_{j-\frac{1}{2}}) \right)^\top \cdot \mathbf{V}(x_{j-\frac{1}{2}}) \\
 & \quad - \Delta t_n \int_{I_j} \left(0, \frac{g}{2} (b_h^D)^2 - gC_0 b_h^D \right)^\top \cdot \mathbf{V}_x dx.
 \end{aligned} \tag{25}$$

Now we can combine (15), (22), (24) and (25), and get

$$\int_{I_j} \widehat{\mathbf{U}}_h^{n+1,C} \cdot \mathbf{V} dx = \int_{I_j} (C_0, 0)^\top \cdot \mathbf{V} dx. \tag{26}$$

By further taking $\mathbf{V} = \widehat{\mathbf{U}}_h^{n+1,C} - (C_0, 0)^\top \in \mathcal{V}_h^{C,k}$, we obtain $\widehat{\mathbf{U}}_h^{n+1,C} = (C_0, 0)^\top$. On the other hand, with $\widehat{\mathbf{U}}_h^{n+1,C} = (C_0, 0)^\top$, Eq. (20) becomes

$$f(h_h^{n+1,C}; b_h^C) = h_h^{n+1,C} \left(1 + \frac{1}{2} h_h^{n+1,C} (b_h^C)_{xx} \right).$$

This, together with assumptions (A1) and (A2), ensures the unique solvability of the finite element discretization (19) and therefore implies $u_h^{n+1,C} = 0$. Similarly, we can establish $\widehat{\mathbf{U}}_h^{n+1,D} = (C_0, 0)^\top$ and $u_h^{n+1,D} = 0$. This completes the proof. \square

3.2.3. High order time discretizations, nonlinear limiter, boundary conditions, dry elements and linear solver

To achieve better accuracy in time, strong stability preserving (SSP) high order time discretizations [16] will be used. Such discretizations can be written as a convex combination of the forward Euler method, and therefore the full scheme with a high order SSP time discretization is still well-balanced.

When CDG methods are applied to nonlinear problems, nonlinear limiters are often needed. In this work, we observed that nonlinear limiters are needed when the solution of the Green–Naghdi equations develops sharp gradients and when the bottom topography is variable. In these cases, we use the total variation bounded (TVB) minmod slope limiter with parameter $M = 1$ [10]. The limiter is applied to $(\eta = h + b, hK)^\top$ as suggested in [43] and is implemented component by component.

It is known that the numerical treatment of boundary conditions is of great importance in wave simulations. This is especially so when the computational domain is truncated from the physical domain. Effort needs to be made to reduce reflected waves from the computational domain boundary. In the present work, for the generating boundary condition (as in Section 5.2.3), ghost elements are introduced adjacent to the boundary. In these elements, the L^2 projection of the prescribed incident wave is applied to implement the boundary condition. For outgoing boundary conditions, ghost elements are used as well, with the same polynomial representation as in the adjacent interior element. In our numerical experiments, when outgoing boundary conditions are specified, the computational domain is also chosen large enough so that the nontrivial part of solutions remains away from the boundary and thus possible wave reflection has negligible effects in the region of interest. This simple treatment works effectively at the expense of high computational cost, although it is not much of an issue in the one-dimensional case. In general however, it should be replaced by more efficient boundary treatments [9].

To treat dry areas (as in Section 5.2.4), we first identify elements where the water height satisfies $h \leq 10^{-13}$. We then assign $u = K = 0$ for these dry elements.

When the continuous finite element method is applied to the elliptic equation, one needs to solve a linear algebraic system at each discrete time or at each Runge–Kutta inner stage. In the present work, we simply employ the Gaussian elimination method as the linear solver.

4. Linear dispersion analysis

In this section, we carry out linear dispersion analysis for both the (reformulated) Green–Naghdi system and versions of the proposed numerical scheme. To allow for a sufficiently tractable analysis and illustrate the dispersion properties of the models, we focus on the flat-bottom case.

4.1. Linear dispersion analysis for the continuous model

We first derive the linear dispersion relation for the reformulated Green–Naghdi system (8)–(9). Linearizing this nonlinear system about the trivial solution $h = h_0 > 0$, $u = u_0$ (both h_0 and u_0 are real constants) and $hK = h_0 u_0$, i.e. looking for solutions of the form

$$h = h_0 + \tilde{h}, \quad u = u_0 + \tilde{u}, \quad hK = h_0 u_0 + \tilde{h}\tilde{K},$$

where $(\tilde{h}, \tilde{hK}, \tilde{u})$ are small perturbations, and retaining only linear terms in $(\tilde{h}, \tilde{hK}, \tilde{u})$, we obtain

$$\begin{cases} \tilde{h}_t + h_0 \tilde{u}_x + u_0 \tilde{h}_x = 0, \\ (\tilde{hK})_t + gh_0 \tilde{h}_x + u_0 (\tilde{hK})_x + h_0 u_0 \tilde{u}_x = 0, \end{cases} \tag{27}$$

with

$$\tilde{hK} = -\frac{1}{3} h_0^3 \tilde{u}_{xx} + h_0 \tilde{u} + u_0 \tilde{h}. \tag{28}$$

Then looking for perturbations as plane waves

$$\begin{pmatrix} \tilde{h} \\ \tilde{hK} \\ \tilde{u} \end{pmatrix} = \begin{pmatrix} \hat{h} \\ \hat{hK} \\ \hat{u} \end{pmatrix} e^{i(\kappa x - \omega t)},$$

we end up with the linear system

$$\begin{cases} -i(\omega - u_0 \kappa) \hat{h} + ih_0 \kappa \hat{u} = 0, \\ -i(\omega - u_0 \kappa) \hat{hK} + igh_0 \kappa \hat{h} + ih_0 u_0 \kappa \hat{u} = 0, \end{cases} \tag{29}$$

with

$$\hat{hK} = \left(1 + \frac{1}{3} h_0^2 \kappa^2\right) h_0 \hat{u} + u_0 \hat{h}. \tag{30}$$

Here κ is the wavenumber and ω is the frequency of the perturbations. Without loss of generality, κ is taken to be real and positive. By substituting \hat{hK} from (30) into (29), this system is reduced to

$$\begin{pmatrix} -(\omega - u_0 \kappa) & h_0 \kappa \\ g\kappa - \frac{u_0}{h_0}(\omega - u_0 \kappa) & -(\omega - u_0 \kappa)\left(1 + \frac{1}{3} h_0^2 \kappa^2\right) + u_0 \kappa \end{pmatrix} \begin{pmatrix} \hat{h} \\ \hat{u} \end{pmatrix} = \begin{pmatrix} 0 \\ 0 \end{pmatrix},$$

and it has nontrivial solutions if the determinant of the coefficient matrix is zero, i.e.

$$(\omega - u_0 \kappa)^2 \left(1 + \frac{1}{3} h_0^2 \kappa^2\right) - gh_0 \kappa^2 = 0,$$

or, alternatively,

$$\omega = \omega_{\pm} := \left(u_0 \pm \sqrt{gh_0 \left(1 + \frac{1}{3} h_0^2 \kappa^2\right)^{-1}}\right) \kappa. \tag{31}$$

This gives the linear dispersion relation for the reformulated Green–Naghdi equations (8)–(9). Note that both ω_+ and ω_- are real according to (31). We also carry out the linear dispersion analysis for the original Green–Naghdi equations (3)–(4) and get the same relation (31). Due to similarity in the calculation, the details are omitted here.

In Fig. 1, we compare the linear dispersion relation (31) of the Green–Naghdi equations and that of the full water wave problem in finite depth,

$$(\omega - u_0 \kappa)^2 = g\kappa \tanh(h_0 \kappa),$$

with $g = 1$, $h_0 = 1$ and $u_0 = 0$. As expected, the two curves coincide in the long-wave limit $\kappa \rightarrow 0$. Furthermore, the linear phase speed corresponding to (31) is

$$c = \left|\frac{\omega}{\kappa}\right| = \sqrt{gh_0 \left(1 + \frac{1}{3} h_0^2 \kappa^2\right)^{-1}},$$

for $u_0 = 0$, which consistently tends to the shallow-water limit $c = \sqrt{gh_0}$ as $\kappa \rightarrow 0$, and remains bounded (i.e. $c \rightarrow 0$) as $\kappa \rightarrow \infty$.

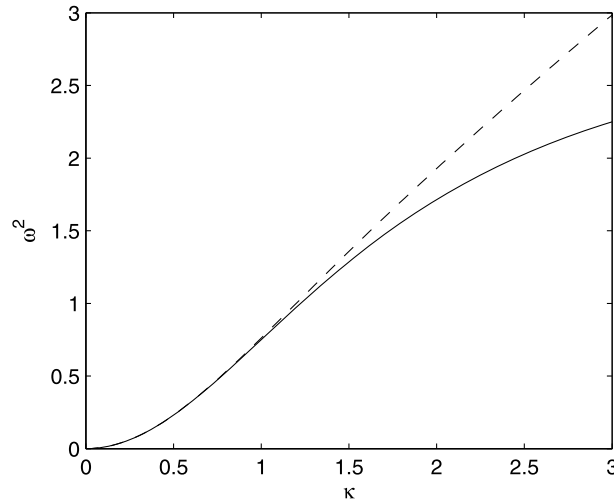


Fig. 1. Comparison between the linear dispersion relation (31) of the Green–Naghdi equations (solid line) and the exact linear dispersion relation of the full water wave problem (dashed line), with $g = 1$, $h_0 = 1$ and $u_0 = 0$.

4.2. Linear dispersion analysis for the discrete model

We now derive the linear dispersion relation for the proposed scheme in its semi-discrete form in time. The mesh is assumed to be uniform with mesh size Δx . Because such analysis is more involved algebraically for higher order cases, we will focus on low order versions of the proposed scheme, as described below.

To approximate (27) for $(\tilde{h}, \tilde{h}K)$, the first order semi-discrete CDG method is applied. That is, we look for $h_j^C, (hK)_j^C, h_{j-\frac{1}{2}}^D, (hK)_{j-\frac{1}{2}}^D \in \mathbb{R}, \forall j$, satisfying

$$\frac{dh_j^C}{dt} = \frac{1}{2\tau_{\max}}(h_{j-\frac{1}{2}}^D + h_{j+\frac{1}{2}}^D - 2h_j^C) - \frac{1}{\Delta x}(h_0u_{j+\frac{1}{2}}^D + u_0h_{j+\frac{1}{2}}^D) + \frac{1}{\Delta x}(h_0u_{j-\frac{1}{2}}^D + u_0h_{j-\frac{1}{2}}^D), \tag{32}$$

$$\begin{aligned} \frac{d(hK)_j^C}{dt} &= \frac{1}{2\tau_{\max}}((hK)_{j-\frac{1}{2}}^D + (hK)_{j+\frac{1}{2}}^D - 2(hK)_j^C) - \frac{1}{\Delta x}(gh_0h_{j+\frac{1}{2}}^D + u_0(hK)_{j+\frac{1}{2}}^D + h_0u_0u_{j+\frac{1}{2}}^D) \\ &\quad + \frac{1}{\Delta x}(gh_0h_{j-\frac{1}{2}}^D + u_0(hK)_{j-\frac{1}{2}}^D + h_0u_0u_{j-\frac{1}{2}}^D), \end{aligned} \tag{33}$$

$$\frac{dh_{j-\frac{1}{2}}^D}{dt} = \frac{1}{2\tau_{\max}}(h_{j-1}^C + h_j^C - 2h_{j-\frac{1}{2}}^D) - \frac{1}{\Delta x}(h_0u_j^C + u_0h_j^C) + \frac{1}{\Delta x}(h_0u_{j-1}^C + u_0h_{j-1}^C), \tag{34}$$

$$\begin{aligned} \frac{d(hK)_{j-\frac{1}{2}}^D}{dt} &= \frac{1}{2\tau_{\max}}((hK)_{j-1}^C + (hK)_j^C - 2(hK)_{j-\frac{1}{2}}^D) - \frac{1}{\Delta x}(gh_0h_j^C + u_0(hK)_j^C + h_0u_0u_j^C) \\ &\quad + \frac{1}{\Delta x}(gh_0h_{j-1}^C + u_0(hK)_{j-1}^C + h_0u_0u_{j-1}^C), \end{aligned} \tag{35}$$

where τ_{\max} is the maximal time step over the whole time domain required for numerical stability, see [27].

As for \tilde{u} , since a continuous finite element method is undefined with piecewise constant discrete spaces, the following two cases are considered instead. The first one (Case 1) is to work with (28) exactly. The second one (Case 2) is to approximate \tilde{u} on each mesh by solving (28) with a continuous finite element method using piecewise linear approximations. In this second case, if the standard Lagrangian basis $\{\phi_{j-\frac{1}{2}}^C\}_j$ is used for $\mathcal{W}_h^{C,1}$, namely, $\phi_{j-\frac{1}{2}}^C$ is continuous and piecewise linear, satisfying $\phi_{j-\frac{1}{2}}^C(x_{j'-\frac{1}{2}}) = \delta_{jj'}$ (a similar basis is used for $\mathcal{W}_h^{D,1}$) with $\delta_{jj'}$ being the Kronecker delta, then by explicitly writing the mass and stiffness matrices, the scheme is given as follows. Look for $u_{j+\frac{1}{2}}^C, u_j^D \in \mathbb{R}, \forall j$, such that

$$\left(\frac{h_0^3}{3\Delta x}(-1, 2, -1) + \frac{h_0\Delta x}{6}(1, 4, 1) \right) \begin{pmatrix} u_{j+\frac{3}{2}}^C \\ u_{j+\frac{1}{2}}^C \\ u_{j-\frac{1}{2}}^C \end{pmatrix} = \frac{\Delta x}{2}((hK)_j^C + (hK)_{j+1}^C - u_0(h_j^C + h_{j+1}^C)), \tag{36}$$

$$\left(\frac{h_0^3}{3\Delta x}(-1, 2, -1) + \frac{h_0\Delta x}{6}(1, 4, 1)\right) \begin{pmatrix} u_{j+1}^D \\ u_j^D \\ u_{j-1}^D \end{pmatrix} = \frac{\Delta x}{2}((hK)_{j-\frac{1}{2}}^D + (hK)_{j+\frac{1}{2}}^D - u_0(h_{j-\frac{1}{2}}^D + h_{j+\frac{1}{2}}^D)). \tag{37}$$

In the numerical dispersion analysis, we look for discrete plane wave solutions of the form

$$\begin{pmatrix} h_j^C \\ (hK)_j^C \\ u_j^D \end{pmatrix} = \begin{pmatrix} \hat{h} \\ \hat{hK} \\ \hat{u} \end{pmatrix} e^{i(\kappa x_j - \tilde{\omega}t)}, \quad \begin{pmatrix} h_{j-\frac{1}{2}}^D \\ (hK)_{j-\frac{1}{2}}^D \\ u_{j-\frac{1}{2}}^C \end{pmatrix} = \begin{pmatrix} \hat{h} \\ \hat{hK} \\ \hat{u} \end{pmatrix} e^{i(\kappa x_{j-\frac{1}{2}} - \tilde{\omega}t)}, \tag{38}$$

where, again, κ is the wavenumber and $\tilde{\omega}$ is the frequency. Based on (32)–(35) and denoting $\beta = (\kappa \Delta x)/2$, we find

$$\begin{cases} -i\tilde{\omega}\hat{h} = -\frac{1 - \cos\beta}{\tau_{\max}}\hat{h} - \frac{2i \sin\beta}{\Delta x}(h_0\hat{u} + u_0\hat{h}), \\ -i\tilde{\omega}\hat{hK} = -\frac{1 - \cos\beta}{\tau_{\max}}\hat{hK} - \frac{2i \sin\beta}{\Delta x}(gh_0\hat{h} + u_0\hat{hK} + h_0u_0\hat{u}), \end{cases}$$

which can be rewritten as

$$\begin{pmatrix} \alpha & 0 \\ -2igh_0 \sin\beta & \alpha \end{pmatrix} \begin{pmatrix} \hat{h} \\ \hat{hK} \end{pmatrix} - 2ih_0 \sin\beta \begin{pmatrix} 1 \\ u_0 \end{pmatrix} \hat{u} = \begin{pmatrix} 0 \\ 0 \end{pmatrix}, \tag{39}$$

with

$$\alpha = i(\tilde{\omega}\Delta x - 2u_0 \sin\beta) - \frac{\Delta x}{\tau_{\max}}(1 - \cos\beta).$$

4.2.1. Linear discrete dispersion analysis for Case 1

In Case 1, \tilde{u} is expressed exactly in terms of \tilde{h} and \tilde{hK} based on (28). Combining (39) with (30) yields

$$\left[\begin{pmatrix} \alpha & 0 \\ -2igh_0 \sin\beta & \alpha \end{pmatrix} - 2i\gamma \sin\beta \begin{pmatrix} -u_0 & 1 \\ -u_0^2 & u_0 \end{pmatrix} \right] \begin{pmatrix} \hat{h} \\ \hat{hK} \end{pmatrix} = \begin{pmatrix} 0 \\ 0 \end{pmatrix}, \tag{40}$$

where $\gamma = (1 + \frac{1}{3}h_0^2\kappa^2)^{-1}$. This system has nontrivial solutions if the determinant of the coefficient matrix is zero, which leads to the linear dispersion relation for the numerical scheme,

$$\tilde{\omega} = \tilde{\omega}_r + i\tilde{\omega}_i = \frac{\sin\beta}{\beta}(u_0 \pm \sqrt{gh_0\gamma})\kappa - i\left(\frac{1 - \cos\beta}{\tau_{\max}}\right). \tag{41}$$

Note that the imaginary part $\tilde{\omega}_i = -(1 - \cos\beta)/\tau_{\max}$ is nonpositive and thus the scheme is linearly stable. In particular, when $\tau_{\max} = +\infty$, $\tilde{\omega}_i = 0$ and the scheme is non-dissipative. Moreover, as $\kappa \Delta x \rightarrow 0$,

$$\tilde{\omega}_i = -\frac{(\kappa \Delta x)^2}{8\tau_{\max}} + \frac{1}{\tau_{\max}}O((\kappa \Delta x)^4), \tag{42}$$

$$\tilde{\omega}_r = \frac{\sin\beta}{\beta}\omega = \omega - \frac{\omega(\kappa \Delta x)^2}{24} + O((\kappa \Delta x)^4). \tag{43}$$

Here ω is from the exact linear dispersion relation (31). In actual implementation, τ_{\max} is often taken to be $\tau_{\max} = O(\Delta x)$ [27]. When this happens, the dissipative error $\tilde{\omega}_i$ is of first order and thus dominates. When $\tau_{\max} = +\infty$, this error no longer exists. On the other hand, the dispersive error $\tilde{\omega}_r - \omega$ is always of second order.

4.2.2. Linear discrete dispersion analysis for Case 2

In Case 2, \tilde{u} is approximated by solving (28) with a continuous finite element method on each mesh using piecewise linear approximations. Plugging (38) into (36) (or (37)), we obtain

$$\hat{hK} - u_0\hat{h} = h_0(\gamma(\beta))^{-1}\hat{u}, \tag{44}$$

with

$$\gamma(\beta) = \cos\beta \left(\frac{\kappa^2 h_0^2}{6} \frac{(1 - \cos(2\beta))}{\beta^2} + \frac{2 + \cos(2\beta)}{3} \right)^{-1}. \tag{45}$$

Combining this relation with (39), we have similar results as in (40) and (41) with γ being replaced by $\gamma(\beta)$. Hence one gets the numerical dispersion relation $\tilde{\omega} = \tilde{\omega}_r + i\tilde{\omega}_i$, where $\tilde{\omega}_i$ is the same as for Case 1, and

$$\begin{aligned} \tilde{\omega}_r &= \frac{\sin \beta}{\beta} (u_0 \pm \sqrt{gh_0 \gamma(\beta)}) \kappa \\ &= \omega_{\pm} - \frac{1}{24} \left(\omega_{\pm} \pm \frac{\kappa (h_0^2 \kappa^2 - 3)}{2(h_0^2 \kappa^2 + 3)} \sqrt{gh_0 \left(1 + \frac{1}{3} h_0^2 \kappa^2\right)^{-1}} \right) (\kappa \Delta x)^2 + O((\kappa \Delta x)^4). \end{aligned} \tag{46}$$

Here ω_{\pm} are from the exact linear dispersion relation (31). Again, the dispersive error is second order accurate in Case 2.

Note that, in the numerical dispersion analysis, we use the same $\tilde{\omega}$ in (38) for the solutions on both meshes. This can be justified by the fact that in the low order scheme considered in this section, $\dots h_{j-\frac{1}{2}}^D, h_j^C, h_{j+\frac{1}{2}}^D, h_{j+1}^C \dots$ (similarly to other numerical unknowns) can be regarded as one function evaluated at $\dots, x_{j-\frac{1}{2}}, x_j, x_{j+\frac{1}{2}}, x_{j+1} \dots$. The superscripts C and D do not essentially contribute to the scheme hence the analysis.

5. Numerical examples

In this section, numerical experiments are presented to demonstrate the performance of the Green–Naghdi model and the proposed methods. We examine in the first part solitary wave solutions of the GN-FB equations, including accuracy tests with varying mesh size, long-time wave propagation (with tests on phase accuracy for P^1 and P^2 approximations, on conservation of mass and energy), as well as simulations of head-on and overtaking collisions. In these flat-bottom cases, the CDG–FE method proposed in Section 3.2.1 is applied, without the need for the well-balanced treatment nor the TVB limiter. In the second part, we test the well-balanced CDG–FE method proposed in Section 3.2.2 on the GN-NFB equations. We consider cases of stationary solutions over continuous and discontinuous bottom topographies, as well as the generation of higher harmonics in Stokes waves over a submerged bar and the runup of solitary waves on a sloping beach. Only the simulations of harmonic generation over a bar (Section 5.2.3) and runup of breaking solitary waves on a slope (Section 5.2.4), in which steep solutions develop, require using the TVB limiter to ensure numerical stability. For the other variable-bottom tests, the limiter is not needed.

All simulations were performed with both P^1 and P^2 approximations. For convenience, we only show P^2 results in most tests, and all reported results are from numerical solutions on the primal mesh $\{I_j\}_j$. In all simulations, we used a uniform mesh with constant mesh size Δx , and the third-order TVD Runge–Kutta method for time discretization [10], with the time step dynamically determined by

$$\frac{C_{cfl} \Delta x}{\max(|u|)}, \tag{47}$$

where the CFL number C_{cfl} was taken as 0.16 for both P^1 and P^2 approximations. We point out that formula (47) may lead to large time steps in cases where the velocity is or close to zero, which thus promotes numerical instabilities. Therefore we used a constant time step $C_{cfl} \Delta x$, instead of (47), for the examples in Sections 5.2.1–5.2.3. No instability was experienced with (47) in other examples. We also set $\theta_n = 1$ for computational efficiency and non-dimensionalize the equations such that the gravitational constant g is unity.

The GN-FB model has an exact solitary wave solution [35] given by

$$\begin{cases} h(x, t) = h_1 + (h_2 - h_1) \operatorname{sech}^2 \left(\frac{x - Dt}{2} \sqrt{\frac{3(h_2 - h_1)}{h_2 h_1^2}} \right), \\ u(x, t) = D \left(1 - \frac{h_1}{h(x, t)} \right), \end{cases} \tag{48}$$

where h_1 is the typical water depth, h_2 corresponds to the solitary wave crest and $D = \sqrt{gh_2}$ is the wave speed. Unless stated otherwise, this expression will be used as initial conditions in our numerical simulations. In particular, it will serve as the reference solution to evaluate numerical errors in our accuracy tests.

5.1. Examples with flat bottom

In this first part, we consider numerical solutions of the GN-FB model (4), based on the CDG–FE method described in Section 3.2.1.

5.1.1. Accuracy tests

As a first example, we test the high order accuracy of the CDG–FE method by varying the mesh size. This situation describes a solitary wave initially located at $x = 0$ and propagating in the positive x -direction. We set initial conditions with $h_1 = 1$ and $h_2 = 2.25$ in (48). The computational domain is $\Omega = [-45, 45]$ and the final time is $t = |\Omega|/D$ at which the soliton has traveled one length of the domain. Periodic boundary conditions are used. We present L^2 errors and orders of accuracy for h and u in Table 1. The results show that the CDG–FE method is $(k + 1)$ st order accurate for P^k with $k = 1, 2$ and therefore it is optimal with respect to the approximation properties of the discrete spaces. Regarding the numerical

Table 1
 L^2 errors and orders of accuracy of (h, u) for solitary waves with $h_2 = 2.25$.

Mesh	h		u	
	L^2 error	Order	L^2 error	Order
		P^1		
100	3.78E-01	–	2.66E-01	–
200	1.08E-01	1.81	6.78E-02	1.97
400	1.93E-02	2.49	1.19E-02	2.51
800	3.44E-03	2.49	2.11E-03	2.49
1600	6.77E-04	2.35	4.15E-04	2.35
3200	1.46E-04	2.21	8.98E-05	2.21
		P^2		
100	2.45E-01	–	1.60E-01	–
200	3.87E-02	2.66	2.42E-02	2.72
400	5.06E-03	2.93	3.16E-03	2.94
800	6.40E-04	2.98	3.99E-04	2.98
1600	8.04E-05	2.99	5.01E-05	2.99
3200	1.01E-05	3.00	6.27E-06	3.00

Table 2
 L^2 errors and orders of accuracy of (h, u) for solitary waves with $h_2 = 10$.

Mesh	h		u	
	L^2 error	Order	L^2 error	Order
		P^2		
100	3.36E-01	–	1.04E-01	–
200	2.90E-02	3.53	9.18E-03	3.51
400	3.07E-03	3.23	9.58E-04	3.26
800	3.87E-04	2.99	1.18E-04	3.01
1600	5.05E-05	2.94	1.53E-05	2.95

errors presented in Table 1 and in other tables below, we use the 5-point Gaussian quadrature formula to evaluate the corresponding integral on each element.

We also test the impact of solitary wave nonlinearity on the convergence rate of the scheme. For this purpose, we take $h_1 = 1$ and $h_2 = 10$ in (48) with the same setting as above. L^2 errors for the P^2 approximation are presented in Table 2, showing the optimal order of accuracy with respect to the approximation properties of the discrete spaces. We have also tried larger values of h_2 up to 50 and still observed the optimal order of accuracy for the CDG-FE method.

5.1.2. Long-time propagation of solitary waves

The second example addresses the performance of the CDG-FE method when simulating the long-time propagation of a single solitary wave. We use the same setting as in the previous test ($h_1 = 1$ and $h_2 = 2.25$), and the computational domain is discretized with 1000 elements. We compute the solution up to $t = 900$. In this setting, the solitary wave has a uniform speed $D = 1.5$, and therefore it has traveled 15 lengths of the domain at the final time.

The wave profiles at $t = 0$ and $t = 900$ are presented in Fig. 2. To graphical accuracy, we see that the wave shape and height are well preserved during this long-time propagation. Moreover, the P^2 approximation displays much better phase accuracy than the P^1 result. For a more quantitative assessment, we depict the time evolution of the relative errors on total mass and energy for the P^2 approximation in Fig. 3. These errors are computed relative to the values at $t = 0$. The total mass and energy associated with the GN-FB model are defined by [23]

$$M = \int_{\Omega} h \, dx, \quad E = \int_{\Omega} \left(\frac{1}{2}gh^2 + \frac{1}{6}h^3u_x^2 \right) dx. \tag{49}$$

The integrals in (49) are evaluated numerically by using the 5-point Gaussian quadrature formula in each mesh element. Fig. 3 indicates that both mass and energy are overall well conserved throughout the computation. Mass conservation is especially well satisfied, within $O(10^{-14})$ (near machine precision), while energy conservation is of $O(10^{-5})$ and tends to slowly deteriorate in time.

5.1.3. Head-on collision of two solitary waves

The third example concerns the collision between two solitary waves traveling in opposite directions (head-on collision). Numerical and experimental investigations of this problem have been carried out by many researchers using different mathematical models and numerical methods. During the head-on collision, the solution rises to an amplitude larger than the sum of the amplitudes of the two incident solitary waves. After the collision, two principal waves emerge, with amplitudes

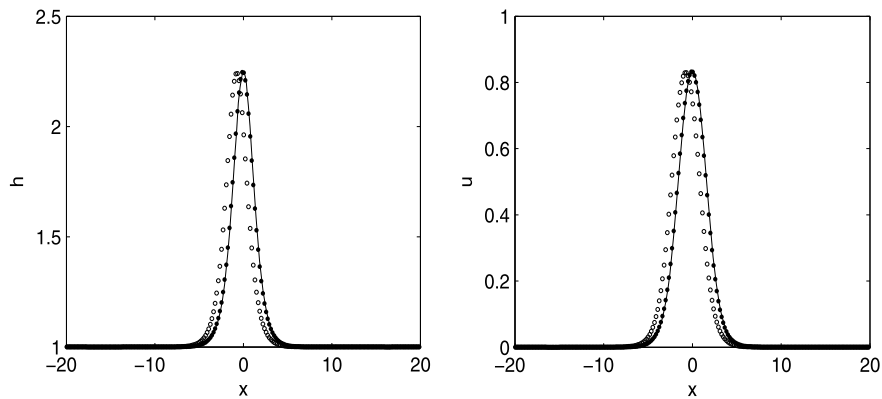


Fig. 2. Comparison of solitary wave profiles at $t = 0$ (solid line) and $t = 900$ (circles: P^1 , dots: P^2). The left panel represents h while the right panel represents u .

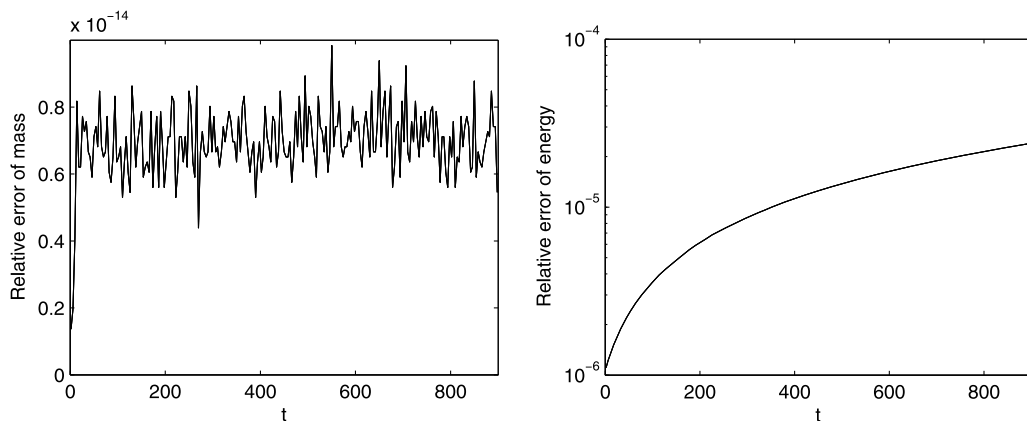


Fig. 3. Time evolution of relative errors in mass (left) and energy (right) for the long-time propagation of a solitary wave.

initially significantly below their initial amplitudes. They then relax, regain amplitude, and finally return to the form of two solitary waves separating from each other. As a result of this collision, the amplitudes of the two resulting solitary waves are slightly smaller than the initial amplitudes, their centers are slightly retarded from the trajectories of the incoming centers (the phase lag), and there is a small residual from the inelastic nature of the interaction.

We start the computation with two solitary waves of different amplitudes. The left wave is initially located at $x = 25$ with $h_2 = 1.213$ in (48) and propagates to the right, while the right wave is initially located at $x = 47$ with $h_2 = 1.243$ and propagates to the left. The typical water depth is $h_1 = 1$ and the computational domain is $[0, 72]$ discretized into 1000 elements. Outgoing boundary conditions are specified in this case.

Snapshots of the head-on collision at $t = 7, 10.5, 11.2, 11.9, 12.5, 14.4, 16.8$ and 24.4 are shown in Fig. 4. Our numerical results (in dimensional units) are compared with experimental data together with simulations of the full Euler equations based on a high order spectral method [11]. Overall, there is a very good agreement among these three sets of results. It can be observed that the two initial solitary waves move toward each other and merge together, reaching a maximum height at $t = 11.2$. The water height then begins to decrease before two principal waves re-emerge. Finally they return to the form of two separating solitary waves, with small dispersive tails (also called residual waves) behind them. Zooming in the GN-FB solution at $t = 24.4$ clearly reveals these residual waves in Fig. 5, which is consistent with those observed in numerical simulations of the Euler equations [11].

5.1.4. Overtaking collision of two solitary waves

The last example with flat bottom is devoted to the investigation of the collision between two solitary waves traveling in the same direction. An overtaking collision consists of the larger solitary wave catching up and interacting with the smaller one, subsequently passing on and separating from it, and leaving a residual wave trailing both resulting solitary waves. Because this interaction occurs between waves with velocities of the same sign, it takes place over a long time interval, in contrast to the case of head-on collisions. Solitary waves resulting from an overtaking collision have slightly modified amplitudes and velocities, but they experience a substantial positive phase shift. Here the computational domain is $[0, 72]$ with periodic boundary conditions and discretized into 500 elements.

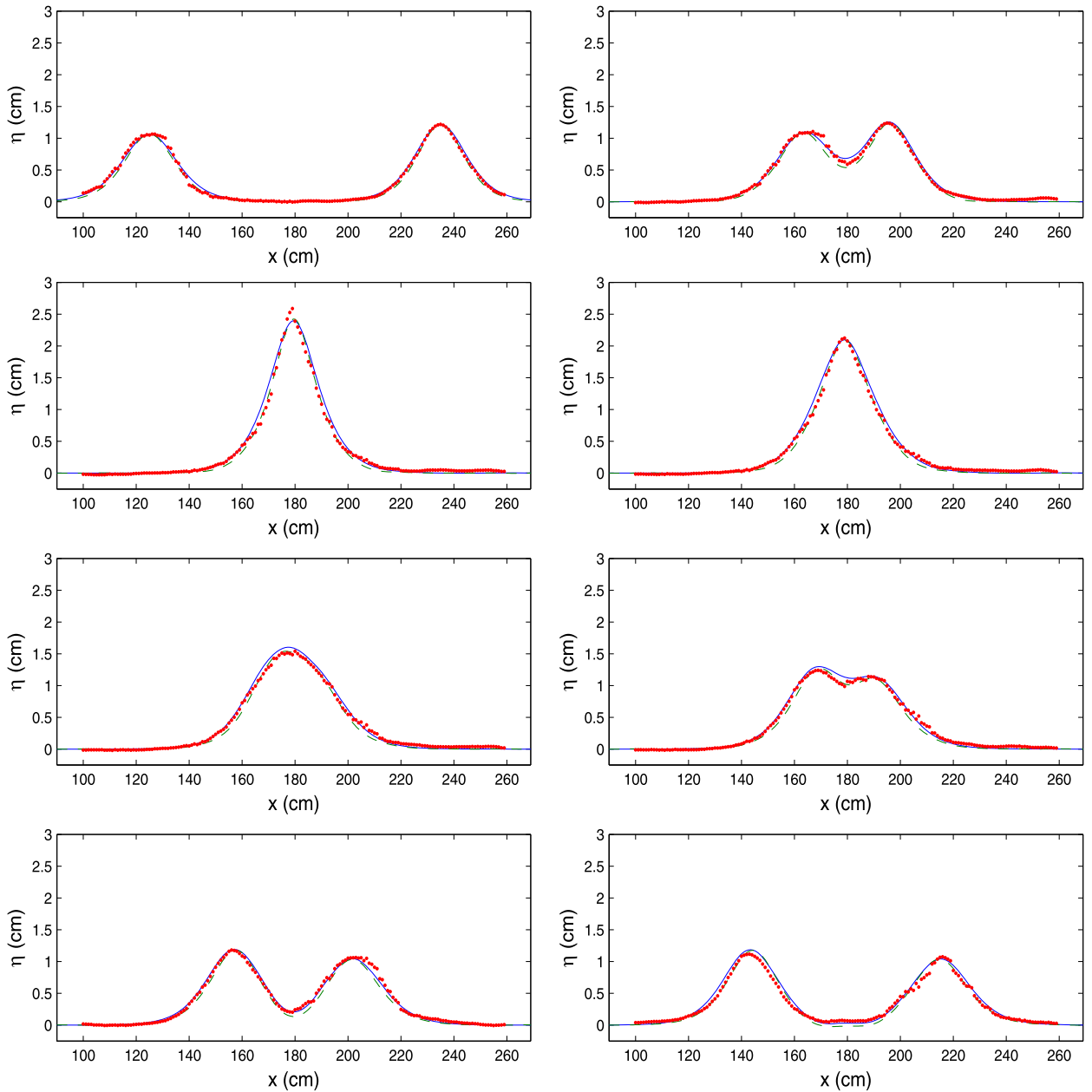


Fig. 4. Head-on collision of two solitary waves of height 1.213 (1.063 cm, left) and 1.243 (1.217 cm, right) at (from left to right, from top to bottom) $t = 7$ (18.29993 s), 10.5 (18.80067 s), 11.2 (19.05257 s), 11.9 (19.10173 s), 12.5 (19.15088 s), 14.4 (19.19389 s), 16.8 (19.32905 s) and 24.4 (19.50109 s). Experimental data are in dots, full Euler results are in dashed line [11] and GN-FB results are in solid line. Numbers in parentheses next to the height and time data are the corresponding dimensional values. The label η denotes the water surface.

Snapshots of the overtaking collision at $t = 0.0, 36.40, 49.05, 58.09, 65.79, 78.40, 92.47$ and 117.64 are shown in Fig. 6. Our numerical results are again compared with experimental data together with simulations of the full Euler equations [11]. Note that the comparison is displayed in a reference frame that aligns the centers of mass of the interacting waves (see [11] for further explanations). There are clear discrepancies regarding the amplitude and relative phase of the solitary waves. For the GN-FB solution, the collision process seems to occur faster and the emerging waves seem to be of larger amplitude than for the other two sets of results. Nevertheless, there is a good agreement in the overall features of the interaction. These discrepancies are most likely due to the GN-FB model (which has weakly dispersive properties) rather than the numerical method. Because an overtaking collision takes place over a relatively long period of time, accumulated dispersive effects are expected to play a significant role. Furthermore, the much lower wave amplitudes shown by the experimental data after the collision are attributable to dissipative mechanisms in the wave channel, as explained in [11].

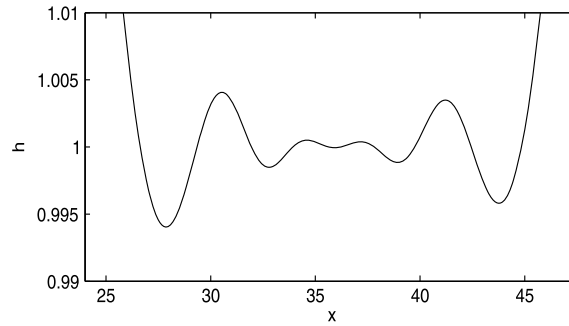


Fig. 5. Zoom-in of dispersive tails generated by the head-on collision of two solitary waves at $t = 24.4$.

5.2. Examples with variable bottom

In this subsection, we demonstrate the ability of the GN-NFB model to describe wave propagation over variable bottom topography. The well-balanced CDG-FE method proposed in Section 3.2.2 is applied to this model.

5.2.1. Stationary solution

We first validate the well-balanced feature, i.e. the ability to preserve still-water steady states, of the proposed well-balanced CDG-FE method in cases of a smoothly variable bottom

$$b(x) = 0.5 - (x - 0.5)^2, \quad (50)$$

and a discontinuous bottom

$$b(x) = \begin{cases} 0.5, & 0.3 \leq x \leq 0.7, \\ 0, & \text{otherwise.} \end{cases} \quad (51)$$

The initial conditions are given by

$$hu = 0, \quad \text{and} \quad h + b = 1. \quad (52)$$

We choose $[0, 1]$ as the computational domain, divided into 50 elements and with outgoing boundary conditions. We compute the solution up to $t = 0.5$ by the standard CDG-FE method, which combines (14) and (19) without the change of unknowns, and by the well-balanced CDG-FE method.

The computed water level $h + b$ and discharge hu are plotted in Figs. 7 and 8, respectively. We see that the standard CDG-FE method fails to maintain the stationary solution (52). After refining the mesh, we cannot observe the solution convergence which is usually attained for the hyperbolic shallow water equations [22]. For the well-balanced CDG-FE method, however, the stationary solution is well preserved, and this is also the case on a coarser mesh (say, 10 elements). To further demonstrate that the well-balanced scheme indeed preserves the still-water stationary solution exactly (i.e. up to machine precision), we performed the computation in both single and double precision. The corresponding L^1 and L^∞ errors on the water height h and discharge hu are listed in Table 3. Their values have orders of magnitude consistent with machine single- and double-precision, thus verifying the well-balanced property.

5.2.2. Accuracy tests

In this example, we test the high order accuracy of the well-balanced CDG-FE method for a smoothly variable solution. We choose the following smooth functions for the initial conditions,

$$\eta = h + b = 1.25 \operatorname{sech}^2(0.65x), \quad u = 0, \quad (53)$$

and for the bottom profile,

$$b(x) = 0.5e^{-0.05(x-10)^2} - 1. \quad (54)$$

The computational domain is $[-30, 30]$ with outgoing boundary conditions. The final time is $t = 1$ at which the solution is still smooth (indeed it tends to steepen in time). Since an exact solution is not known for this problem, we first compute the numerical solution on a very fine mesh with 12800 elements, and then use it as the reference solution to evaluate errors and orders of accuracy for coarser resolutions. We present L^2 errors and orders of accuracy for the water surface η and velocity u in Table 4. Like the standard CDG-FE method, our results also show that the well-balanced CDG-FE method is $(k + 1)$ st order accurate for P^k with $k = 1, 2$ and therefore the well-balanced treatment does not affect the accuracy of the standard CDG-FE method.

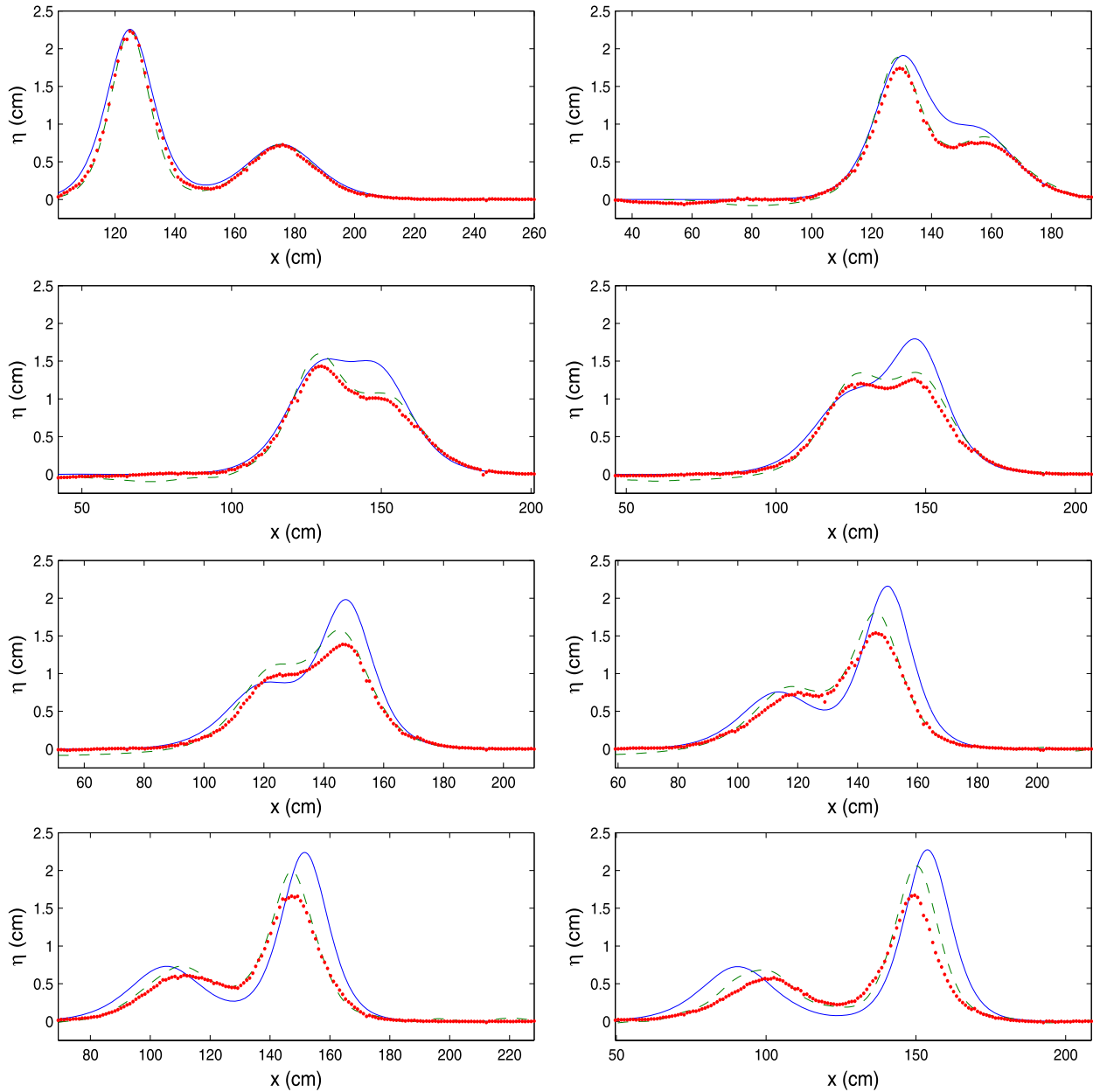


Fig. 6. Overtaking collision of two solitary waves of height 1.456 (2.295 cm, left) and 1.146 (0.730 cm, right) at (from left to right, from top to bottom) $t = 0$ (2.90304 s), 36.40 (5.50196 s), 49.05 (6.40513 s), 58.09 (7.05025 s), 65.79 (7.60014 s), 78.40 (8.50024 s), 92.47 (9.50478 s) and 117.64 (11.30191 s). Experimental data are in dots, full Euler results are in dashed line [11] and GN-FB results are in solid line. Numbers in parentheses next to the height and time data are the corresponding dimensional values. The label η denotes the water surface.

5.2.3. Harmonic generation over a submerged bar

This example describes the propagation of Stokes waves over a submerged bar. As shown in experimental work [12], regular waves decompose into higher-frequency free waves as they propagate past a submerged bar. As the waves travel up the front slope of the bar, higher harmonics are generated due to nonlinear interactions, causing the waves to steepen. These harmonics are then released as free waves on the downslope, producing an irregular pattern behind the bar. This experiment is particularly difficult to simulate because it includes nonlinear interactions and requires accurate propagation of waves in both deep and shallow water over a wide range of depths. Therefore it has often been used as a discriminating test case for nonlinear models of surface wave propagation over variable bottom [12,20,6].

Here we also compare our well-balanced GN-NFB results with experimental data of Dingemans [12]. The computational domain is [0 m, 120 m] with mesh size 1/40. The bottom variation (in meters) is defined by

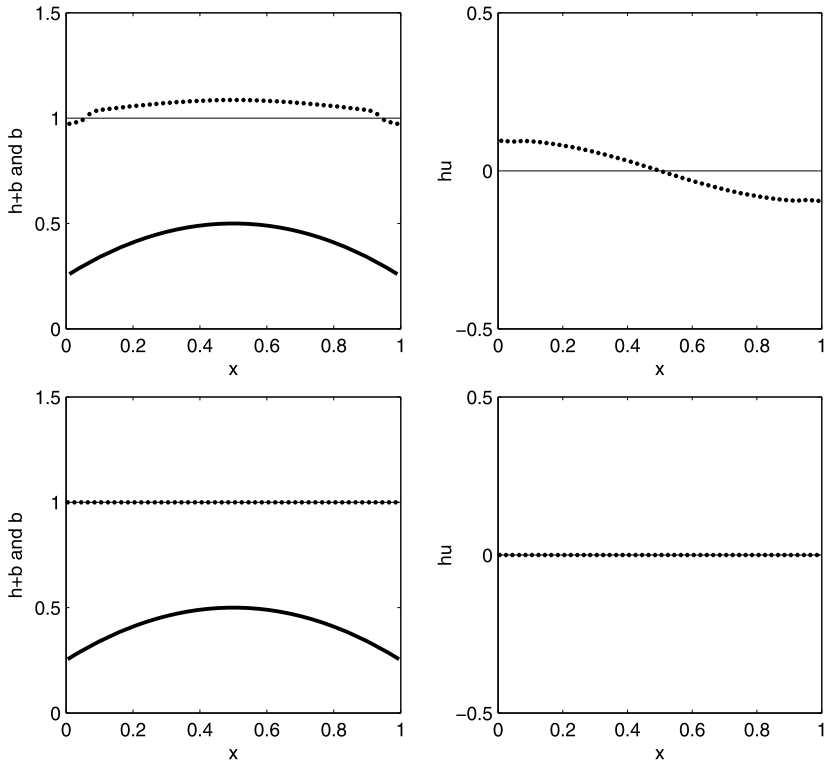


Fig. 7. Numerical results for the stationary solution over a smoothly variable bottom at $t = 0.5$. Dots: numerical solution, thin solid line: exact solution, thick solid line: bottom profile. Top: standard CDG-FE method, bottom: well-balanced CDG-FE method.

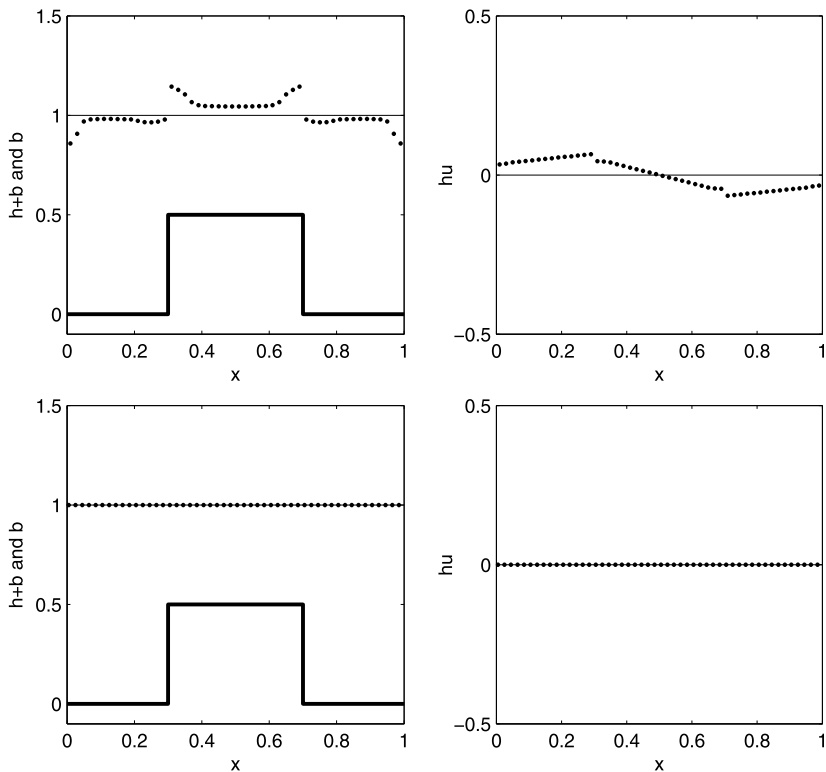


Fig. 8. Numerical results for the stationary solution over a discontinuous bottom at $t = 0.5$. Dots: numerical solution, thin solid line: exact solution, thick solid line: bottom profile. Top: standard CDG-FE method, bottom: well-balanced CDG-FE method.

Table 3
 L^1 and L^∞ errors on (h, hu) for the stationary solution at $t = 0.5$.

Precision	h		hu	
	L^1 error	L^∞ error	L^1 error	L^∞ error
	smooth bottom			
single	3.24E-10	3.52E-09	2.81E-08	1.87E-07
double	2.50E-16	4.04E-15	3.42E-17	2.29E-16
	discontinuous bottom			
single	1.99E-09	1.74E-07	2.98E-08	1.99E-07
double	4.24E-16	1.75E-14	3.05E-17	1.06E-16

Table 4
 L^2 errors and orders of accuracy of (η, u) at $t = 1$.

Mesh	η		u	
	L^2 error	Order	L^2 error	Order
	p^1			
100	7.39E-03	–	6.18E-03	–
200	1.76E-03	2.07	1.25E-03	2.31
400	4.43E-04	1.99	2.85E-04	2.13
800	1.12E-04	1.98	6.86E-05	2.05
1600	2.83E-05	1.99	1.68E-05	2.03
3200	6.99E-06	2.02	4.07E-06	2.05
	p^2			
100	5.05E-04	–	3.37E-04	–
200	6.31E-05	3.00	4.29E-05	2.97
400	7.90E-06	3.00	5.39E-06	2.99
800	9.86E-07	3.00	6.75E-07	3.00
1600	1.22E-07	3.01	8.44E-08	3.00
3200	1.48E-08	3.04	1.06E-08	3.00

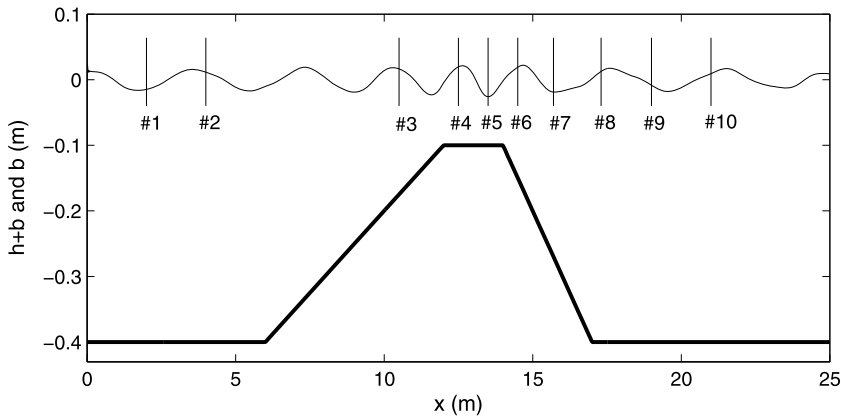


Fig. 9. Experimental set-up and locations of the wave gauges as used in [12].

$$b(x) = \begin{cases} -0.4 + 0.05(x - 6), & 6 \leq x \leq 12, \\ -0.1, & 12 \leq x \leq 14, \\ -0.1 - 0.1(x - 14), & 14 \leq x \leq 17, \\ -0.4, & \text{elsewhere,} \end{cases} \tag{55}$$

and is depicted in Fig. 9 in which we also label the positions of 10 gauges used in [12]. At initial time, $h + b = 0$ and $u = 0$ in the computational domain. The incident wave (entering from the left) is a third-order Stokes wave [14] given by

$$\eta(x, t) = a_0 \cos\left(2\pi\left(\frac{x}{\lambda} - \frac{t}{T_0}\right)\right) + \frac{\pi a_0^2}{\lambda} \cos\left(4\pi\left(\frac{x}{\lambda} - \frac{t}{T_0}\right)\right) - \frac{\pi^2 a_0^3}{2\lambda^2} \left[\cos\left(2\pi\left(\frac{x}{\lambda} - \frac{t}{T_0}\right)\right) - \cos\left(6\pi\left(\frac{x}{\lambda} - \frac{t}{T_0}\right)\right) \right], \tag{56}$$

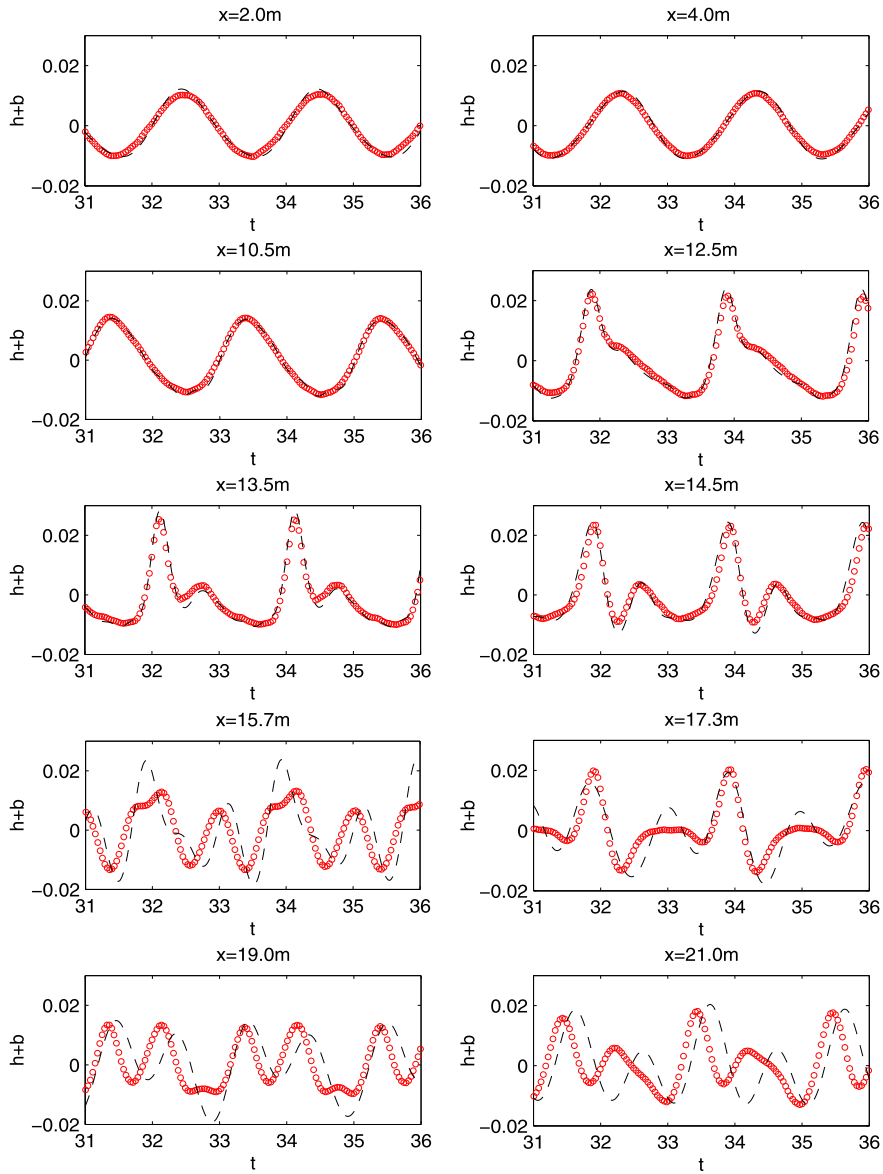


Fig. 10. Time series of surface elevations for waves passing over a submerged bar at $x = 2$ m, 4 m, 10.5 m, 12.5 m, 13.5 m, 14.5 m, 15.7 m, 17.3 m, 19 m and 21 m (from left to right, from top to bottom). Circles: experimental data [12], dashed line: numerical results.

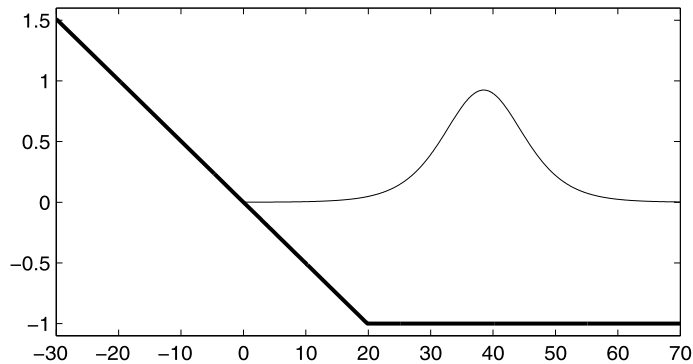


Fig. 11. Sketch for the problem of runup of a solitary wave on a sloping beach.

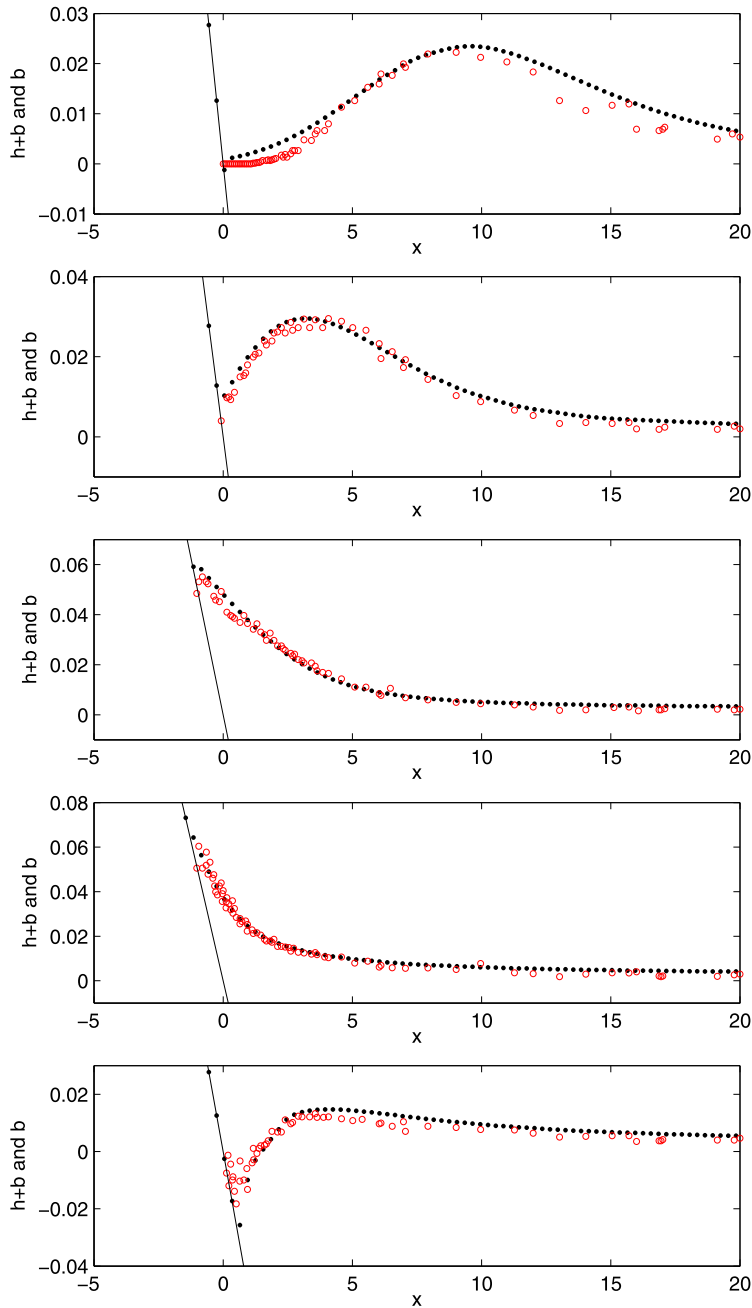


Fig. 12. Runup of a solitary wave with amplitude $a_0 = 0.0185$ at $t = 30, 40, 50, 60, 70$ (from top to bottom). Circles: experimental data [36], dots: Green–Naghdi equations.

where T_0 , a_0 and λ denote the wave period, amplitude and wavelength in scaled units, respectively. We choose $(T_0, a_0, \lambda) = (2.02 \text{ s}, 0.01 \text{ m}, 3.73 \text{ m})$ corresponding to one of the experiments in [12]. An outgoing condition is applied at the right boundary.

Time histories of the water surface at the 10 gauges are shown in Fig. 10. The time origin has been shifted so that the numerical results match the measurements for the first gauge at $x = 2 \text{ m}$. Overall, both sets of data compare well together. However, discrepancies in amplitude and phase can be observed for gauges beyond the crest of the bar (i.e. $x \geq 15.7 \text{ m}$). These discrepancies again should be attributed to the weakly dispersive character of the GN-NFB model. As described above, the wave pattern on the downslope of the bar (and beyond) consists of high-frequency free waves which are highly dispersive waves. Recently, a new Green–Naghdi system with improved dispersive properties has shown better performance in comparison with the experimental data [6].

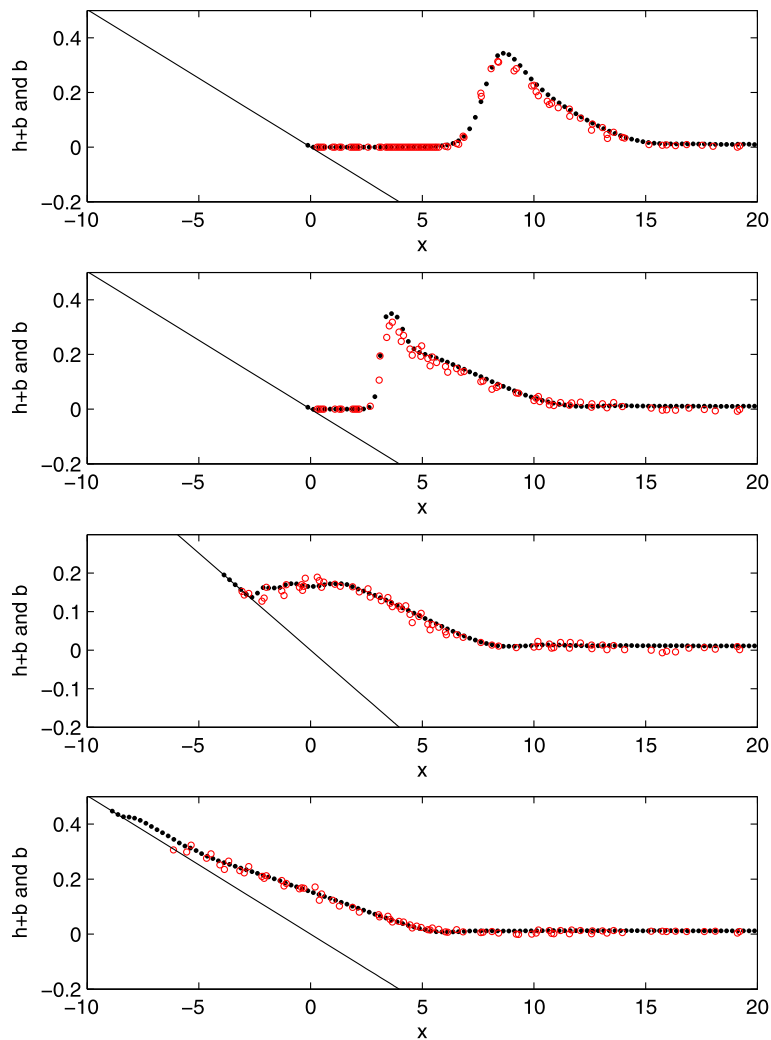


Fig. 13. Runup of a solitary wave with amplitude $a_0 = 0.28$ at $t = 15, 20, 25, 30$ (from top to bottom). Circles: experimental data [36], dots: Green–Naghdi equations.

5.2.4. Runup of solitary waves on a slope

In this example, we examine the runup of solitary waves on a mild slope of 1 : 19.85 following experimental work of Synolakis [36]. The bottom slope is specified by

$$b(x) = \begin{cases} -x \tan \beta, & x \leq \cot \beta, \\ -1, & x > \cot \beta, \end{cases} \tag{57}$$

with $\beta = 2.884^\circ$ and is depicted in Fig. 11. We first consider the runup of a solitary wave of small amplitude $a_0 = 0.0185$ with $h_1 = 1$ and $h_2 = 1.0185$ in (48). The solution is initially located at $x = 38.5$ and travels to the left up the sloping beach. The computational domain is $[-30, 70]$ divided into 1000 elements and with outgoing boundary conditions.

A sequence of wave profiles is presented in Fig. 12. To illustrate the performance of the GN-NFB model and of the numerical method, we also plot experimental data from [36] for comparison. We see that the wave profiles computed by the Green–Naghdi model match the experimental data well during both runup and rundown phases. Discrepancies observed at $t = 70$ near the shoreline (where the sloping beach and the water surface meet) are likely due to viscous effects, as stated in [36].

Finally, we investigate the runup of a breaking solitary wave with larger amplitude $a_0 = 0.28$ ($h_1 = 1$ and $h_2 = 1.28$). The solution is initially located at $x = 25.6$ and again travels to the left. We show a sequence of wave profiles in Fig. 13 which again includes a comparison with experimental data from [36]. We also see that the wave profiles computed by the Green–Naghdi model match the experimental data well up to the runup phase. In particular, the solitary wave shoaling and steepening are well reproduced by the numerical solution.

6. Conclusions

In this paper, we develop a family of high order numerical methods which couple the central discontinuous Galerkin methods and the continuous finite element methods for solving one-dimensional Green–Naghdi equations with flat bottom topography, and their well-balanced counterparts for solving one-dimensional Green–Naghdi equations with variable bottom topography. These methods are based on reformulating the original system into a conservation/balance law coupled with an elliptic equation. Linear dispersion analysis is performed for both the reformulated Green–Naghdi system and versions of the proposed numerical scheme. Numerical experiments are presented to demonstrate the accuracy, robustness and well-balanced property of the proposed methods, as well as the capability of the Green–Naghdi equations to model a wide range of shallow water wave phenomena.

In the future, we will consider the inclusion of the positivity-preserving treatment in the well-balanced CDG framework for shallow water and Green–Naghdi equations. The reformulation technique by introducing the new unknown K can also be extended to two dimensions in a straightforward manner.

Acknowledgements

Maojun Li is partially supported by China Scholarship Council, and he is also grateful to the Department of Mathematical Sciences at Rensselaer Polytechnic Institute for its hospitality during the academic year 2011–2012. Philippe Guyenne is partially supported by a grant from the Simons Foundation (No. 246170) and he also would like to thank the Institute for Advanced Study (Princeton, NJ) for its hospitality during the academic year 2011–2012. Fengyan Li is partially supported by NSF CAREER award DMS-0847241 and an Alfred P. Sloan Research Fellowship. Liwei Xu is partially supported by NSF RTG Grant DMS-0636358 and the Youth 100 Plan start-up grant of Chongqing University (No. 0208001104413) in China.

References

- [1] Y. Agnon, P.A. Madsen, H.A. Schäffer, A new approach to high order Boussinesq models, *J. Fluid Mech.* 399 (1999) 319–333.
- [2] A. Bermudez, M.E. Vazquez, Upwind methods for hyperbolic conservation laws with source terms, *Comput. Fluids* 23 (1994) 1049–1071.
- [3] P. Bonneton, E. Barthélemy, F. Chazel, R. Cienfuegos, D. Lannes, F. Marche, M. Tissier, Recent advances in Serre–Green Naghdi modelling for wave transformation, breaking and runup processes, *Eur. J. Mech. B, Fluids* 30 (2011) 589–597.
- [4] P. Bonneton, F. Chazel, D. Lannes, F. Marche, M. Tissier, A splitting approach for the fully nonlinear and weakly dispersive Green–Naghdi model, *J. Comput. Phys.* 230 (2011) 1479–1498.
- [5] R. Camassa, D.D. Holm, C.D. Levermore, Long-time effects of bottom topography in shallow water, *Physica D* 98 (1996) 258–286.
- [6] F. Chazel, D. Lannes, F. Marche, Numerical simulation of strongly nonlinear and dispersive waves using a Green–Naghdi model, *J. Sci. Comput.* 48 (2011) 105–116.
- [7] D.Y. Choi, C.H. Wu, C.-C. Young, An efficient curvilinear non-hydrostatic model for simulating surface water waves, *Int. J. Numer. Methods Fluids* 66 (2011) 1093–1115.
- [8] R. Cienfuegos, E. Barthélemy, P. Bonneton, A fourth-order compact finite volume scheme for fully nonlinear and weakly dispersive Boussinesq-type equations. Part I: Model development and analysis, *Int. J. Numer. Methods Fluids* 51 (2006) 1217–1253.
- [9] R. Cienfuegos, E. Barthélemy, P. Bonneton, A fourth-order compact finite volume scheme for fully nonlinear and weakly dispersive Boussinesq-type equations. Part II: Boundary conditions and validation, *Int. J. Numer. Methods Fluids* 53 (2007) 1423–1455.
- [10] B. Cockburn, C.-W. Shu, The Runge–Kutta discontinuous Galerkin method for conservation laws V: Multidimensional systems, *J. Comput. Phys.* 141 (1998) 199–224.
- [11] W. Craig, P. Guyenne, J. Hammack, D. Henderson, C. Sulem, Solitary water wave interactions, *Phys. Fluids* 18 (2006) 057106.
- [12] M.W. Dingemans, Comparison of computations with Boussinesq-like models and laboratory measurements, Technical report H1684.12, Delft Hydraulics, Delft, The Netherlands, 1994.
- [13] D. Dutykh, T. Katsaounis, D. Mitsotakis, Finite volume schemes for dispersive wave propagation and runup, *J. Comput. Phys.* 230 (2011) 3035–3061.
- [14] J.D. Fenton, A fifth-order Stokes theory for steady waves, *J. Waterway Port Coast. Ocean Eng.* 111 (1985) 216–234.
- [15] M.F. Gobbi, J.T. Kirby, G. Wei, A fully nonlinear Boussinesq model for surface waves. II. Extension to $O(kh^4)$, *J. Fluid Mech.* 405 (2000) 181–210.
- [16] S. Gottlieb, C.-W. Shu, E. Tadmor, Strong stability preserving high order time discretization methods, *SIAM Rev.* 43 (2001) 89–112.
- [17] A.E. Green, P.M. Naghdi, A derivation of equations for wave propagation in water of variable depth, *J. Fluid Mech.* 78 (1976) 237–246.
- [18] S.T. Grilli, P. Guyenne, F. Dias, A fully nonlinear model for three-dimensional overturning waves over an arbitrary bottom, *Int. J. Numer. Methods Fluids* 35 (2001) 829–867.
- [19] P. Guyenne, S.T. Grilli, Numerical study of three-dimensional overturning waves in shallow water, *J. Fluid Mech.* 547 (2006) 361–388.
- [20] P. Guyenne, D.P. Nicholls, A high-order spectral method for nonlinear water waves over moving bottom topography, *SIAM J. Sci. Comput.* 30 (2007) 81–101.
- [21] S. Israwi, Derivation and analysis of a new 2D Green–Naghdi system, *Nonlinearity* 23 (2010) 2889–2904.
- [22] M. Li, P. Guyenne, F. Li, L. Xu, High order positivity-preserving well-balanced central discontinuous Galerkin methods for the nonlinear shallow water equations, in preparation.
- [23] O. Le Métayer, S. Gavriluk, S. Hank, A numerical scheme for the Green–Naghdi model, *J. Comput. Phys.* 229 (2010) 2034–2045.
- [24] F. Li, S. Yakovlev, A central discontinuous Galerkin method for Hamilton–Jacobi equations, *J. Sci. Comput.* 45 (2010) 404–428.
- [25] F. Li, L. Xu, Arbitrary order exactly divergence-free central discontinuous Galerkin methods for ideal MHD equations, *J. Comput. Phys.* 231 (2012) 2655–2675.
- [26] F. Li, L. Xu, S. Yakovlev, Central discontinuous Galerkin methods for ideal MHD equations with exactly divergence-free magnetic field, *J. Comput. Phys.* 230 (2011) 4828–4847.
- [27] Y. Liu, C.-W. Shu, E. Tadmor, M. Zhang, Central discontinuous Galerkin methods on overlapping cells with a nonoscillatory hierarchical reconstruction, *SIAM J. Numer. Anal.* 45 (2007) 2442–2467.
- [28] Y. Liu, C.-W. Shu, E. Tadmor, M. Zhang, Central local discontinuous Galerkin methods on overlapping cells for diffusion equations, *ESAIM Math. Model. Numer. Anal.* 45 (2011) 1009–1032.
- [29] J. Miles, R. Salmon, Weakly dispersive nonlinear gravity waves, *J. Fluid Mech.* 157 (1985) 519–531.

- [30] S. Noelle, Y. Xing, C.-W. Shu, High order well-balanced finite volume WENO schemes for shallow water equation with moving water, *J. Comput. Phys.* 226 (2007) 29–58.
- [31] J.D. Pearce, J.G. Esler, A pseudo-spectral algorithm and test cases for the numerical solution of the two-dimensional rotating Green–Naghdi shallow water equations, *J. Comput. Phys.* 229 (2010) 7594–7608.
- [32] F.J. Seabra-Santos, D.P. Renouard, A.M. Temperville, Numerical and experimental study of transformation of a solitary wave over a shelf or isolated obstacle, *J. Fluid Mech.* 176 (1987) 117–134.
- [33] F. Serre, Contribution à l'étude des écoulements permanents et variables dans les canaux, *Houille Blanche* 8 (1953) 374–388.
- [34] F. Shi, J.T. Kirby, J.C. Harris, J.D. Geiman, S.T. Grilli, A high-order adaptive time-stepping TVD solver for Boussinesq modeling of breaking waves and coastal inundation, *Ocean Model.* 43–44 (2012) 36–51.
- [35] C.H. Su, C.S. Gardner, Korteweg–de Vries equation and generalizations. III. Derivation of the Korteweg–de Vries equation and Burgers equation, *J. Math. Phys.* 10 (1969) 536–539.
- [36] C.E. Synolakis, The runup of solitary waves, *J. Fluid Mech.* 185 (1987) 523–545.
- [37] S. Vukovic, L. Sopta, ENO and WENO schemes with the exact conservation property for one-dimensional shallow water equations, *J. Comput. Phys.* 179 (2002) 593–621.
- [38] S. Vukovic, N. Crnjarić-Zic, L. Sopta, WENO schemes for balance laws with spatially varying flux, *J. Comput. Phys.* 199 (2004) 87–109.
- [39] Y. Xing, C.-W. Shu, High order finite difference WENO schemes with the exact conservation property for the shallow water equations, *J. Comput. Phys.* 208 (2005) 206–227.
- [40] Y. Xing, C.-W. Shu, High order well-balanced finite volume WENO schemes and discontinuous Galerkin methods for a class of hyperbolic systems with source terms, *J. Comput. Phys.* 214 (2006) 567–598.
- [41] Y. Xing, C.-W. Shu, High order well-balanced finite difference WENO schemes for a class of hyperbolic systems with source terms, *J. Sci. Comput.* 27 (2006) 477–494.
- [42] Y. Xing, C.-W. Shu, A new approach of high order well-balanced finite volume WENO schemes and discontinuous Galerkin methods for a class of hyperbolic systems with source terms, *Commun. Comput. Phys.* 1 (2006) 100–134.
- [43] Y. Xing, X. Zhang, C.-W. Shu, Positivity-preserving high order well-balanced discontinuous Galerkin methods for the shallow water equations, *Adv. Water Resour.* 33 (2010) 1476–1493.
- [44] L. Xu, P. Guyenne, Numerical simulation of three-dimensional nonlinear water waves, *J. Comput. Phys.* 228 (2009) 8446–8466.